

The Multi-Fluid Plasma Model: Derivation, Context, & Computational Solution

Uri Shumlak

current students:

Allyson Kim, Robert Lilly, Sean Miller, Noah Reddell, Eder Sousa

former students:

Shaun Gilliam, Ammar Hakim, John Loverich, Weston Lowrie,
Eric Meier, Bhuvana Srinivasan

Aerospace & Energetics Research Program
University of Washington, Seattle

Computational Methods in High Energy Density Plasmas
7 – 11 May 2012

Presentation Outline

- Derivation of the Multi-Fluid Plasma Model
 - Moments of Boltzmann Eq. (5M or 13M systems)
 - Eigenvalues and timescales of the model
 - Collision terms for scattering & reacting interactions
- Context for the Model: Relation to MHD & Kinetic Models
 - Asymptotic approximations & modification of dispersion relations
- Computational Solution Methods
 - Balance law form of governing equations, approx. Riemann fluxes
 - Finite Volume & Finite Element spatial discretizations
 - Addressing divergence errors in Maxwell's equations
 - Non-reflecting open boundary conditions
- Applications of Multi-Fluid Plasma Code
 - Benchmarking to analytical dispersion, GEM challenge, & UQ
 - Drift instabilities in Z-pinch & FRCs, experiment anomalous resistivity
 - Sheath formation dynamics in plasma generation

Derivation of the multi-fluid plasma model

Discrete model accounting for each constituent particle is not particularly useful for the mathematical treatment of realistic plasmas. Instead an average is performed to give a statistical description.

Plasmas may be most accurately modeled using kinetic theory, distribution functions, $f_s(\mathbf{x}, \mathbf{v}, t)$, governed by a Boltzmann equation

$$\frac{\partial f_s}{\partial t} + \mathbf{v} \cdot \frac{\partial f_s}{\partial \mathbf{x}} + \frac{q_s}{m_s} (\mathbf{E} + \mathbf{v} \times \mathbf{B}) \cdot \frac{\partial f_s}{\partial \mathbf{v}} = \frac{\partial f_s}{\partial t} \Big|_{\text{collisions}}$$

for each plasma species s , e.g. i^+ , e^- , n , and Maxwell's equations.

However, the model fills six dimensional space.

Simpler plasma models are generated by taking moments over velocity space of the Boltzmann equation and the distribution function for each species, which gives the **Multi-Fluid Plasma** model.

Principal variables for the multi-fluid plasma model

The principal fluid variables for each species are derived by computing moments of the distribution functions as

$$(1) \quad \rho_s = m_s \int f_s(\mathbf{v}) d\mathbf{v}$$

$$(2) \quad \rho_s \mathbf{u}_s = m_s \int \mathbf{v} f_s(\mathbf{v}) d\mathbf{v}$$

$$(3) \quad \mathbf{P}_s = m_s \int \mathbf{w} \mathbf{w} f_s(\mathbf{v}) d\mathbf{v} \quad \text{where} \quad \mathbf{w} \equiv \mathbf{v} - \mathbf{u}_s$$

$$(4) \quad \mathbf{H}_s = m_s \int \mathbf{w} \mathbf{w} \mathbf{w} f_s(\mathbf{v}) d\mathbf{v}$$

⋮

5M model evolves variables: Eqs.(1,2) & tensor contraction of Eq.(3).

$$p_s = \rho_s T_s = \frac{1}{3} m_s \int w^2 f_s(\mathbf{v}) d\mathbf{v}$$

13M model evolves variables: Eqs.(1,2,3) & tensor contraction of Eq.(4).

$$\mathbf{h}_s = \frac{1}{2} m_s \int w^2 \mathbf{w} f_s(\mathbf{v}) d\mathbf{v}$$

All variables with a physical meaning are retained in the 13M model.*

Governing equations for the multi-fluid plasma model

The governing equations that evolve the principal fluid variables are derived by computing moments of the Boltzmann equation as

$$m_s \int \mathbf{v}^n \frac{\partial f_s}{\partial t} d\mathbf{v} + m_s \int \mathbf{v}^{n+1} \cdot \frac{\partial f_s}{\partial \mathbf{x}} d\mathbf{v} + q_s \int \mathbf{v}^n (\mathbf{E} + \mathbf{v} \times \mathbf{B}) \cdot \frac{\partial f_s}{\partial \mathbf{v}} d\mathbf{v} = m_s \int \mathbf{v}^n \frac{\partial f_s}{\partial t} \Big|_c d\mathbf{v}$$

Assuming appropriate smoothness properties of f_s and manipulating the integrals gives the governing equation for evolving the moment variable, term A .

$$\frac{\partial}{\partial t} \underbrace{\left(m_s \int \mathbf{v}^n f_s d\mathbf{v} \right)}_A + \frac{\partial}{\partial \mathbf{x}} \cdot \underbrace{\left(m_s \int \mathbf{v}^{n+1} f_s d\mathbf{v} \right)}_B + \dots$$

Each moment of the Boltzmann equation gives an equation for the moment variable given by term A , and introduces the next higher moment variable given by term B .

Closure Problem: System of equations is truncated by relating higher moment variables to lower moment variables.

Multi-fluid plasma model expressed in balance law form*

The governing equations for the multi-fluid plasma model can be expressed in balance law form with divergence fluxes and sources.

The 5M equations are

$$\frac{\partial \rho_s}{\partial t} + \nabla \cdot (\rho_s \mathbf{u}_s) = \frac{\partial \rho_s}{\partial t} \Big|_{\Gamma}$$

$$\frac{\partial \rho_s \mathbf{u}_s}{\partial t} + \nabla \cdot (\rho_s \mathbf{u}_s \mathbf{u}_s + p_s \mathbf{I} + \Pi_s) = \frac{\rho_s q_s}{m_s} (\mathbf{E} + \mathbf{u}_s \times \mathbf{B}) - \sum_{s^*} \mathbf{R}_{s,s^*} + \frac{\partial \rho_s \mathbf{u}_s}{\partial t} \Big|_{\Gamma}$$

$$\frac{\partial \varepsilon_s}{\partial t} + \nabla \cdot \left(\left((\varepsilon_s + p_s) \mathbf{I} + \Pi_s \right) \cdot \mathbf{u}_s + \mathbf{h}_s \right) = \frac{\rho_s q_s}{m_s} \mathbf{u}_s \cdot \mathbf{E} + \sum_{s^*} Q_{s,s^*} + \frac{\partial \varepsilon_s}{\partial t} \Big|_{\Gamma}$$

where the total energy is $\varepsilon_s \equiv \frac{1}{\gamma - 1} p_s + \frac{1}{2} \rho_s u_s^2$

The fluids are coupled to each other and to the electromagnetic fields through Maxwell's equations and interaction source terms.

Multi-fluid plasma model expressed in balance law form

The 13M model equations have a more complicated form.*

$$\frac{\partial \rho_s}{\partial t} + \nabla \cdot (\rho_s \mathbf{u}_s) = \frac{\partial \rho_s}{\partial t} \Big|_{\Gamma}$$

$$\frac{\partial \rho_s \mathbf{u}_s}{\partial t} + \nabla \cdot (\rho_s \mathbf{u}_s \mathbf{u}_s + \mathbf{P}_s) = \frac{\rho_s q_s}{m_s} (\mathbf{E} + \mathbf{u}_s \times \mathbf{B}) - \sum_{s^*} \mathbf{R}_{s,s^*} + \frac{\partial \rho_s \mathbf{u}_s}{\partial t} \Big|_{\Gamma}$$

$$\frac{\partial}{\partial t} (\rho_s \mathbf{u}_s \mathbf{u}_s + \mathbf{P}_s) + \nabla \cdot (\rho_s \mathbf{u}_s \mathbf{u}_s \mathbf{u}_s + 3\mathbf{P}_s \mathbf{u}_s + \mathbf{H}_s) = \dots$$

$$\frac{\partial}{\partial t} \left(\frac{\rho_s u_s^2 + p_s}{2} \mathbf{u}_s + \mathbf{P}_s \cdot \mathbf{u}_s + \mathbf{h}_s \right) +$$

$$\nabla \cdot \left(\frac{\rho_s u_s^2 + p_s}{2} \mathbf{u}_s \mathbf{u}_s + \frac{\mathbf{P}_s u_s^2}{2} + 2\mathbf{u}_s \mathbf{P}_s \cdot \mathbf{u}_s + 2\mathbf{h}_s \mathbf{u}_s + \mathbf{H}_s \cdot \mathbf{u}_s + \frac{\mathbf{N}_s}{2} \right) = \dots$$

where the reduced fourth moment is defined as $\mathbf{N}_s = m_s \int w^2 \mathbf{w} \mathbf{w} f(\mathbf{v}) d\mathbf{v}$

Multi-fluid plasma model expressed in balance law form

The 13M model equations have a more complicated form.*

$$\frac{\partial \rho_s}{\partial t} + \nabla \cdot (\rho_s \mathbf{u}_s) = \frac{\partial \rho_s}{\partial t} \Big|_{\Gamma}$$

$$\frac{\partial \rho_s \mathbf{u}_s}{\partial t} + \nabla \cdot (\rho_s \mathbf{u}_s \mathbf{u}_s + \mathbf{P}_s) = \frac{\rho_s q_s}{m_s} (\mathbf{E} + \mathbf{u}_s \times \mathbf{B}) - \sum_{s^*} \mathbf{R}_{s,s^*} + \frac{\partial \rho_s \mathbf{u}_s}{\partial t} \Big|_{\Gamma}$$

$$\frac{\partial}{\partial t} (\rho_s \mathbf{u}_s \mathbf{u}_s + \mathbf{P}_s) + \nabla \cdot (\rho_s \mathbf{u}_s \mathbf{u}_s \mathbf{u}_s + 3\mathbf{P}_s \mathbf{u}_s + \mathbf{H}_s) = \dots$$

$$\frac{\partial}{\partial t} \left(\frac{\rho_s u_s^2 + p_s}{2} \mathbf{u}_s + \mathbf{P}_s \cdot \mathbf{u}_s + \mathbf{h}_s \right) + \nabla \cdot \left(\frac{\rho_s u_s^2 + p_s}{2} \mathbf{u}_s \mathbf{u}_s + \frac{\mathbf{P}_s u_s^2}{2} + 2\mathbf{u}_s \mathbf{P}_s \cdot \mathbf{u}_s + 2\mathbf{h}_s \mathbf{u}_s + \mathbf{H}_s \cdot \mathbf{u}_s + \frac{\mathbf{N}_s}{2} \right) = \dots$$

where the reduced fourth moment is defined as $\mathbf{N}_s = m_s \int w^2 \mathbf{w} \mathbf{w} f(\mathbf{v}) d\mathbf{v}$

The equations describe the evolution of the 13M variables: density, momenta, pressure tensor, heat flux.

Field evolution is governed by full Maxwell's equations.

Maxwell's equations govern the evolution of the electromagnetic fields.

The evolution of the electromagnetic fields is coupled to the fluids through source terms for current density and charge density.

$$\frac{\partial \mathbf{B}}{\partial t} + \nabla \times \mathbf{E} = 0$$

$$\frac{\partial \mathbf{E}}{\partial t} - c^2 \nabla \times \mathbf{B} = -\frac{1}{\epsilon_0} \sum_s \frac{\rho_s q_s}{m_s} \mathbf{u}_s$$

In addition to these time-dependent equations, two divergence equations (involutions) must also be satisfied.

$$\nabla \cdot \mathbf{E} = \frac{1}{\epsilon_0} \sum_s \frac{\rho_s q_s}{m_s}$$

$$\nabla \cdot \mathbf{B} = 0$$

Time scales of the multi-fluid plasma model

Combining the governing equations for the fluids with full Maxwell's equations yields the ideal multi-fluid plasma model. The fluid equations can be expressed as

$$\frac{\partial}{\partial t} q + \frac{\partial}{\partial x_k} F_k = S$$

The flux Jacobian, $\mathbf{A} = \partial F_k / \partial q$, is computed and analyzed to give the system's eigenvalues, which demonstrates the system is weakly hyperbolic – real, but repeated, eigenvalues with a complete set of eigenvectors.

For example, the eigenvalues for the two-fluid plasma model (ions, electrons) is

$$\lambda_{\mathbf{A}} = \left(u_{ix}, u_{ix} \pm \sqrt{\gamma T_i / m_i}, u_{ex}, u_{ex} \pm \sqrt{\gamma T_e / m_e} \right)$$

Time scales of the multi-fluid plasma model

Combining the fluid eigenvalues with the characteristics of Maxwell's equations and the source terms provides the characteristic speeds and frequencies, and thereby the time scales.

$$L/u_i, L/u_e, L/v_{Ti}, L/v_A, L/v_{Te}, L/c, 1/\omega_{ci}, 1/\omega_{ce}, 1/\omega_{pi}, 1/\omega_{pe}, \tau_{eq}$$

<i>Time Scales (s)</i>	Lab Plasma, FRC	F Region
$1/\omega_{pe}$	5×10^{-14}	6×10^{-8}
L/c	3×10^{-9}	7×10^{-2}
$1/\omega_{ci}$	10^{-8}	4×10^{-3}
L/v_A	10^{-5}	3×10^1
L/v_{Ti}	4×10^{-5}	10^4
τ_{eq}	10^{-3}	10^5

Large separation of physical time scales makes the equation system stiff.

Collisions appear as source terms of fluid equations

Including scattering and reacting collisions (ionization, recombination, charge exchange) introduces additional source terms that couple the fluids. The governing equations for the electron fluid for an interacting three-fluid model (electron, ion, neutral) becomes*

$$\frac{\partial \rho_e}{\partial t} + \nabla \cdot (\rho_e \mathbf{u}_e) = m_e \Gamma_i^{ion} - m_e \Gamma_n^{rec}$$

$$\frac{\partial \rho_e \mathbf{u}_e}{\partial t} + \nabla \cdot (\rho_e \mathbf{u}_e \mathbf{u}_e + p_e \mathbf{I} + \Pi_e) = -\frac{\rho_e e}{m_e} (\mathbf{E} + \mathbf{u}_e \times \mathbf{B})$$

$$- \mathbf{R}_i^{ie} + \mathbf{R}_e^{en} + m_e \mathbf{u}_n \Gamma_i^{ion} - m_e \mathbf{u}_e \Gamma_n^{rec}$$

$$\begin{aligned} \frac{\partial \varepsilon_e}{\partial t} + \nabla \cdot \left(\left((\varepsilon_e + p_e) \mathbf{I} + \Pi_e \right) \cdot \mathbf{u}_e + \mathbf{h}_e \right) = & -\mathbf{u}_e \cdot \left(\frac{\rho_e e}{m_e} \mathbf{E} + \mathbf{R}_i^{ie} - \mathbf{R}_e^{en} \right) + Q_e^{ie} + Q_e^{en} \\ & + \left(\frac{1}{2} m_e v_n^2 - \phi_{ion} \right) \Gamma_i^{ion} + \frac{m_e}{m_n} Q_n^{ion} - \frac{1}{2} m_e v_e^2 \Gamma_n^{rec} - Q_e^{rec} \end{aligned}$$

where, e.g., $\Gamma_i^{ion} = \int f_n(\mathbf{v}') \int f_e(\mathbf{v}) \sigma_{ion}(|\mathbf{v} - \mathbf{v}'|) |\mathbf{v} - \mathbf{v}'| d\mathbf{v} d\mathbf{v}'$

Context for the multi-fluid plasma model

The only approximation made in the multi-fluid plasma model is local thermodynamic equilibrium of each fluid but not with the other fluids, which allows $T_e \neq T_i \neq T_n$.

The model consists of governing equations for density, momentum, and energy for electrons and ions.

Maxwell's equations complete model. Finite speed of light is included.

Fluids interact through electromagnetic fields and collisions.

Fields are affected by the fluids (currents and charge separations).

Assuming only two fluids, averaging the two fluids, and applying simplifying assumptions yield the single-fluid **MHD** model.

- low frequency, zero electron mass, zero Larmor radius, zero Debye length, zero skin depth

Relation between two-fluid and MHD plasma models

With no loss of generality, the two-fluid equations can be combined to describe a single (center of mass) fluid and a relative drift motion between the fluids, for example, a fluid velocity and current density.

$$\mathbf{v} = \frac{\rho_i \mathbf{u}_i + \rho_e \mathbf{u}_e}{\rho_i + \rho_e} \quad \mathbf{j} = \frac{\rho_i q_i}{m_i} \mathbf{u}_i - \frac{\rho_e e}{m_e} \mathbf{u}_e$$

This represents no loss of generality. Asymptotic approximations are often then applied.

Zero electron inertia:

$$\nabla \cdot (p_e \mathbf{I} + \Pi_e) = -\frac{\rho_e e}{m_e} (\mathbf{E} + \mathbf{u}_e \times \mathbf{B}) - \mathbf{R}_i^{ie}$$

Infinite speed of light:

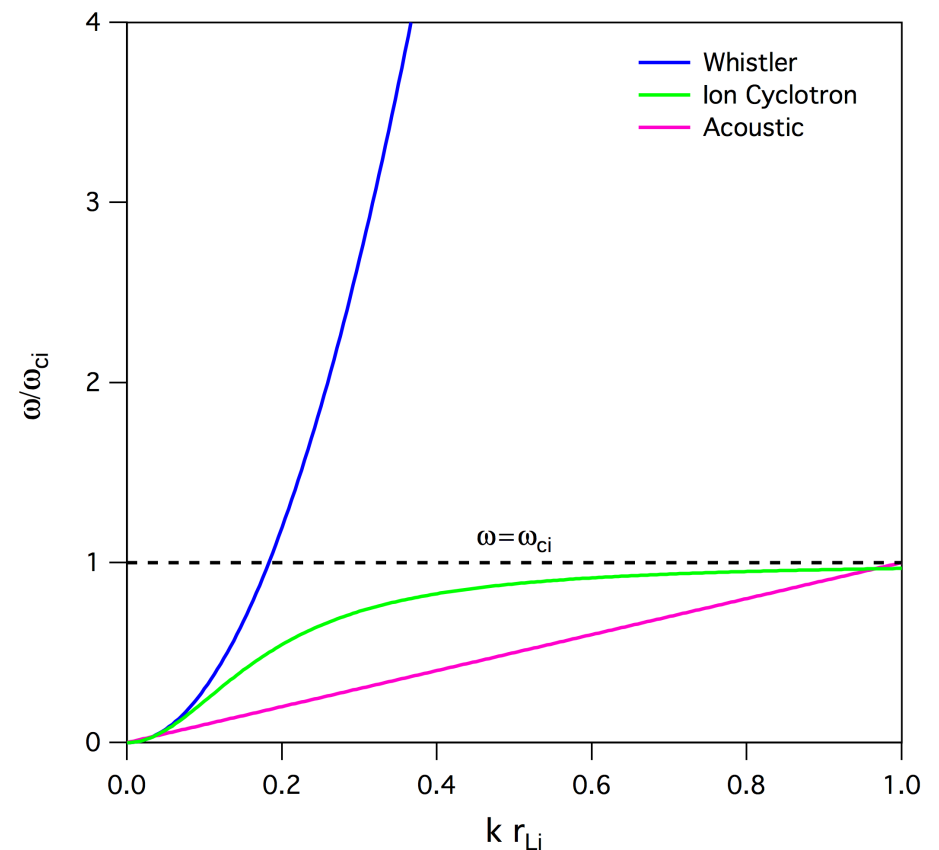
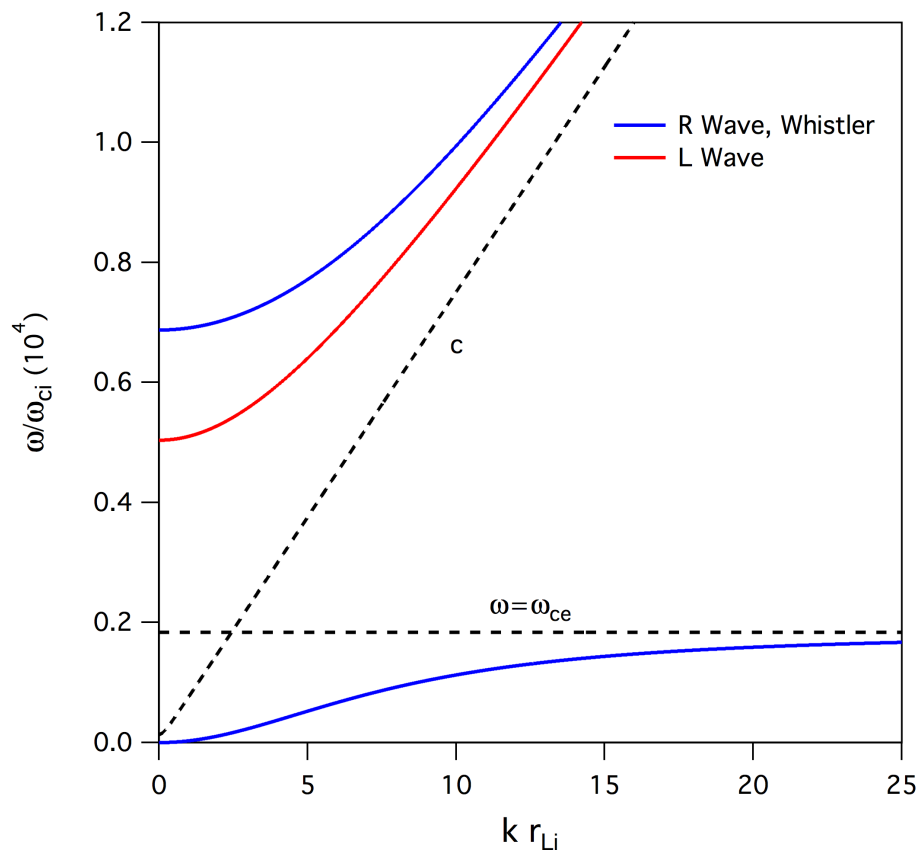
$$\nabla \times \mathbf{B} = \mu_0 \mathbf{j}$$

This yields the Hall-MHD model. (Additional simplifications give resistive MHD and ideal MHD.)

Two-fluid plasma model supports many waves

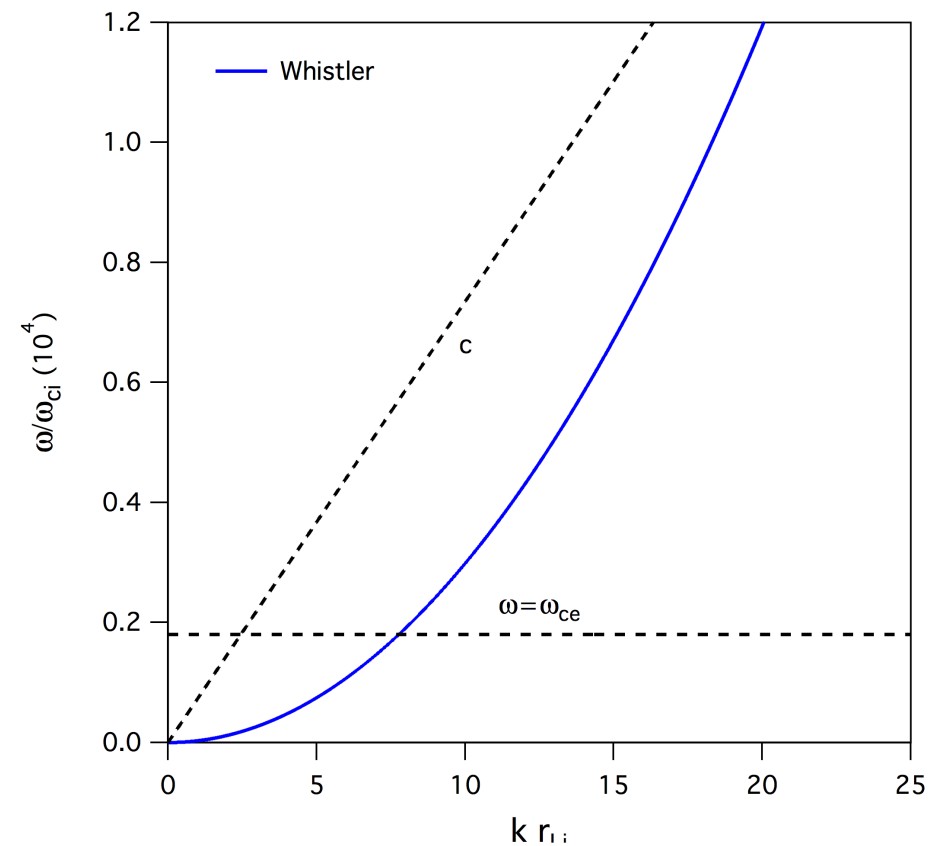
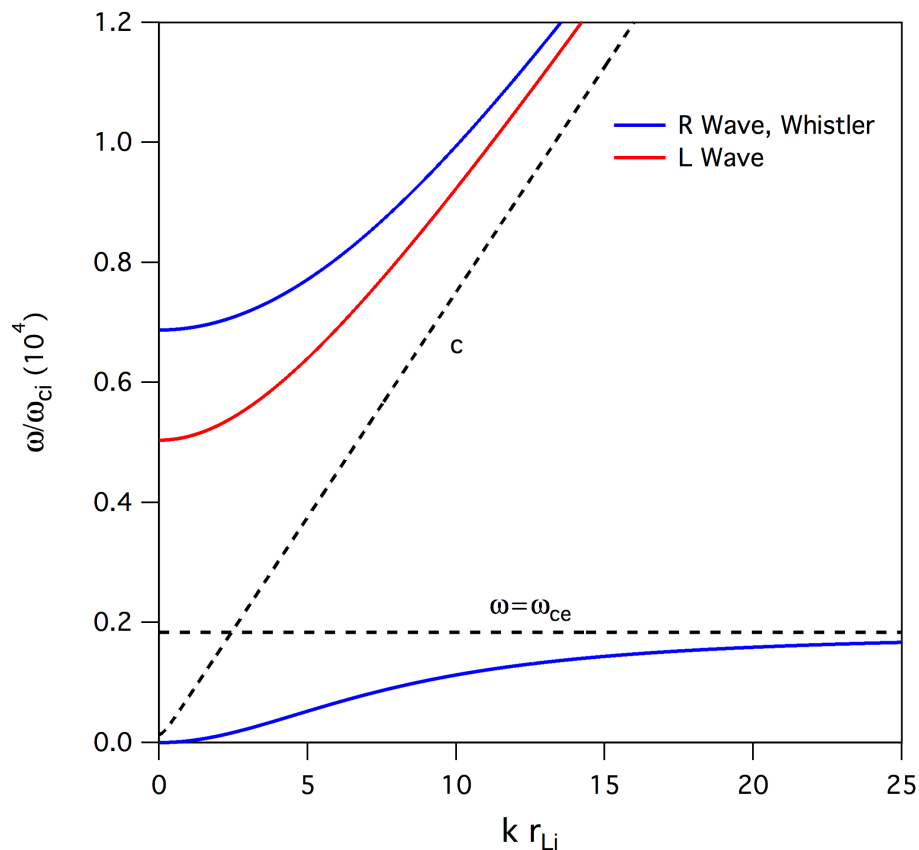
For propagation along the magnetic field, the two-fluid plasma model includes right-hand and left-hand circularly polarized waves, including a lower frequency branch.

Ion waves are also captured in the model.



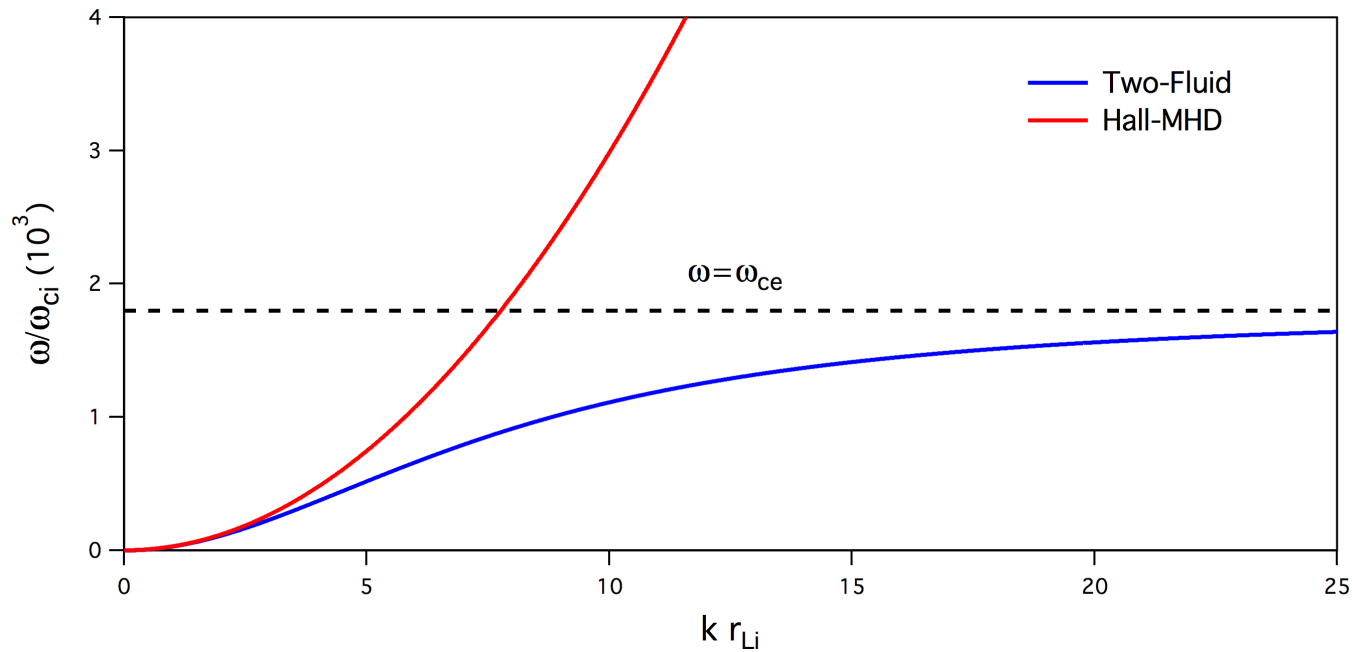
Two-fluid plasma model supports many waves

Two-fluid plasma model must resolve plasma frequency and light propagation. Asymptotic approximations ($m_e \rightarrow 0$, $c \rightarrow \infty$) simplify two-fluid model and yield Hall-MHD model.* At low frequency and long wavelength, Hall MHD dispersion relation matches two-fluid model.



Approximations simplify the model, but lead to difficulty

Two-fluid plasma model must resolve plasma frequency and light propagation. Asymptotic approximations ($m_e \rightarrow 0$, $c \rightarrow \infty$) simplify two-fluid model and yield Hall-MHD model.* At low frequency and long wavelength, Hall MHD dispersion relation matches two-fluid model.



Hall MHD wave misses resonance, diverges from two-fluid wave. Wave velocities approach infinity. System becomes mathematically stiff. Dissipation (hyper-resistivity) is required for stability (truncate k).

Solution methods for the multi-fluid plasma model

The governing equations for the ideal multi-fluid plasma model can be expressed as

$$\frac{\partial q}{\partial t} + \frac{\partial F}{\partial x} = \frac{\partial q}{\partial t} + \mathbf{A} \frac{\partial q}{\partial x} = S$$

Using the eigensystem of the flux Jacobian, an upwind flux can be constructed as an approximate Riemann solver.*

$$\begin{aligned} F_{i+1/2} &= \frac{1}{2} (F_{i+1}^- + F_i^+) \\ &= \frac{1}{2} (F_{i+1} + F_i) - \frac{1}{2} \sum_k l_k (q_{i+1} - q_i) |\lambda_k| r_k \end{aligned}$$

Limiters can be applied to the second term to result in second-order accurate fluxes.

A finite volume scheme can be constructed to solve the equation system. However, the source terms must be tightly coupled to the hyperbolic fluxes. Source splitting or implicit methods can be used.

Higher order solution methods using finite elements

The solution vector is expanded using a set of basis functions as

$$q(\mathbf{r}) = \sum_k q_k v_k(\mathbf{r})$$

The governing equation is then projected using a Galerkin method as

$$\int_{\Omega} v_k \frac{\partial q}{\partial t} dV + \int_{\Omega} v_k \nabla \cdot \mathbf{F} dV = \int_{\Omega} v_k S dV$$

where an integral equation is generated for each basis (test) function.

Integrating by parts and applying the divergence theorem gives

$$\int_{\Omega} v_k \frac{\partial q}{\partial t} dV + \oint_{\partial\Omega} v_k \mathbf{F} \cdot d\mathbf{S} - \int_{\Omega} \mathbf{F} \cdot \nabla v_k dV = \int_{\Omega} v_k S dV$$

This equation is valid in general but is inconvenient for realistic, complicated geometrical domains. Instead, the domain is divided into finite elements and the integral equation is applied to each element with some assumption of continuity at the element boundaries.

Level of continuity between the finite elements

If the solution is assumed to be continuous (C^0), the fluxes are automatically continuous, and the result is the usual finite element method.

$$\int_{\Omega} v_k \frac{\partial q}{\partial t} dV + \oint_{\partial\Omega} v_k \mathbf{F} \cdot d\mathbf{S} - \int_{\Omega} \mathbf{F} \cdot \nabla v_k dV = \int_{\Omega} v_k S dV$$

During assembly of the global system for the simultaneous solution for all q_k^{Ω} , the boundary integral term cancels everywhere except at the domain boundaries. Volume integrals are evaluated by quadrature.

The finite element method works well for many elliptic and parabolic systems on complicated geometries.

Problem: Spurious oscillations occur at discontinuities (shocks) for hyperbolic systems. → Not suitable for many plasma simulations.

Level of continuity between the finite elements

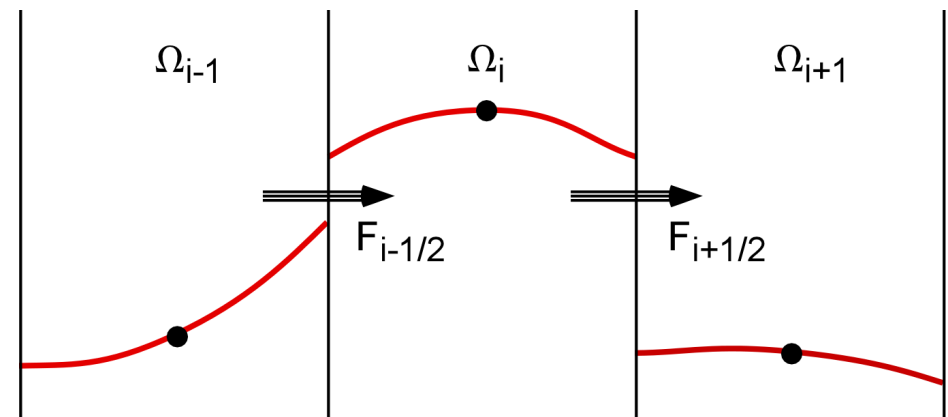
If the solution is allowed to be discontinuous, but with continuous fluxes (C^{-1}), which is the only featured required by the conservation law, the resulting system is the discontinuous Galerkin method.*

$$\int_{\Omega} v_k \frac{\partial q}{\partial t} dV + \oint_{\partial\Omega} v_k \mathbf{F} \cdot d\mathbf{S} - \int_{\Omega} \mathbf{F} \cdot \nabla v_k dV = \int_{\Omega} v_k S dV$$

Fluxes for the surface integral are again evaluated using an upwind method such as an approximate Riemann solver with solution values on either side of the interface.

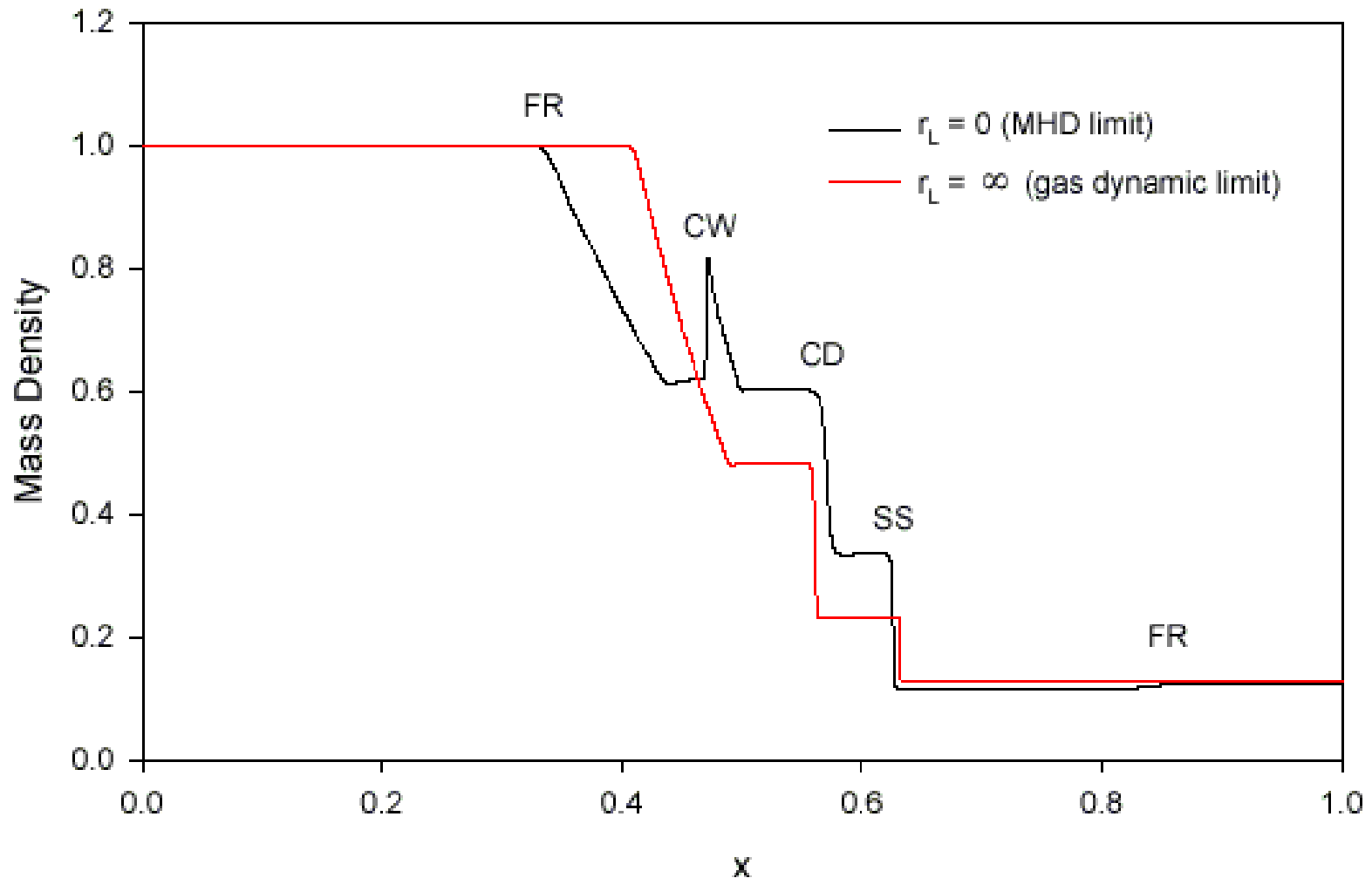
$$\mathbf{F}_{\partial\Omega} = \frac{1}{2}(\mathbf{F}^+ + \mathbf{F}^-) - \frac{1}{2} \sum_k l_k (q^+ - q^-) |\lambda_k| r_k$$

Limiting is often accomplished by locally reducing expansion order.
Time is advanced with a 3rd order TVD, Runge-Kutta method.



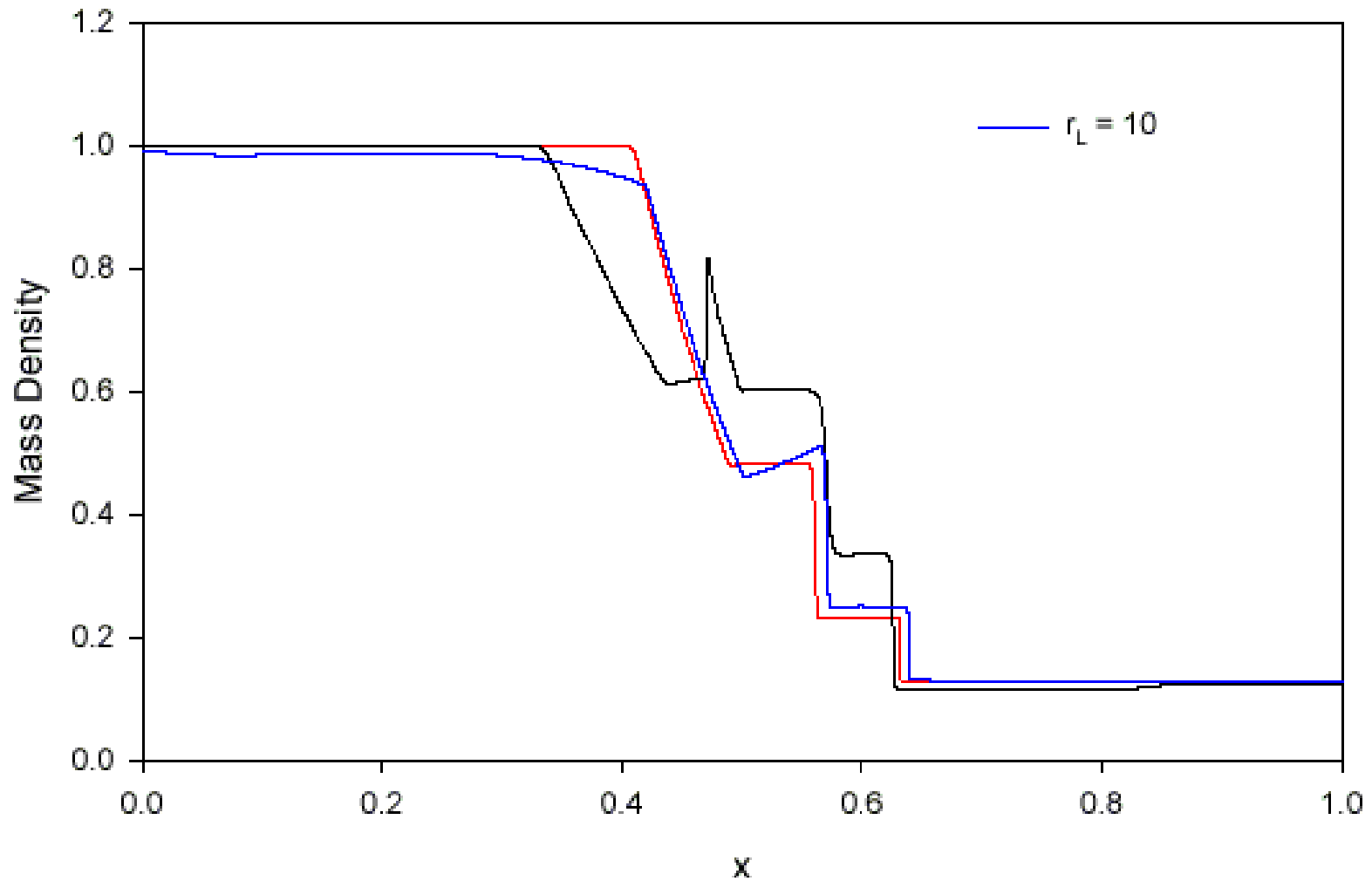
* Cockburn et al., MC **52** (1989); Loverich et al., CCP **9** (2011)

Application/comparison to electromagnetic plasma shock

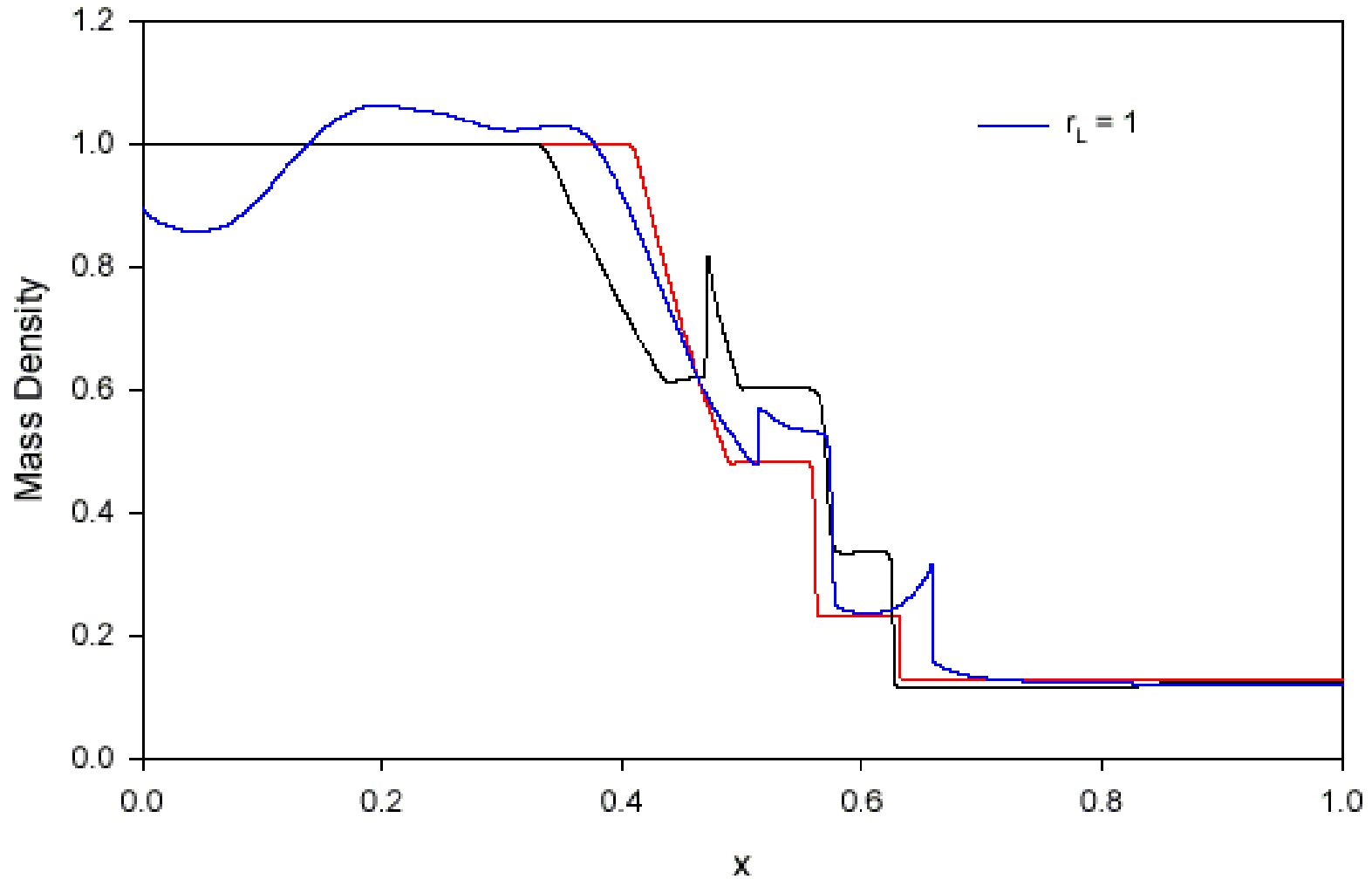


This is a two-fluid plasma model generalization of the MHD shock problem.*

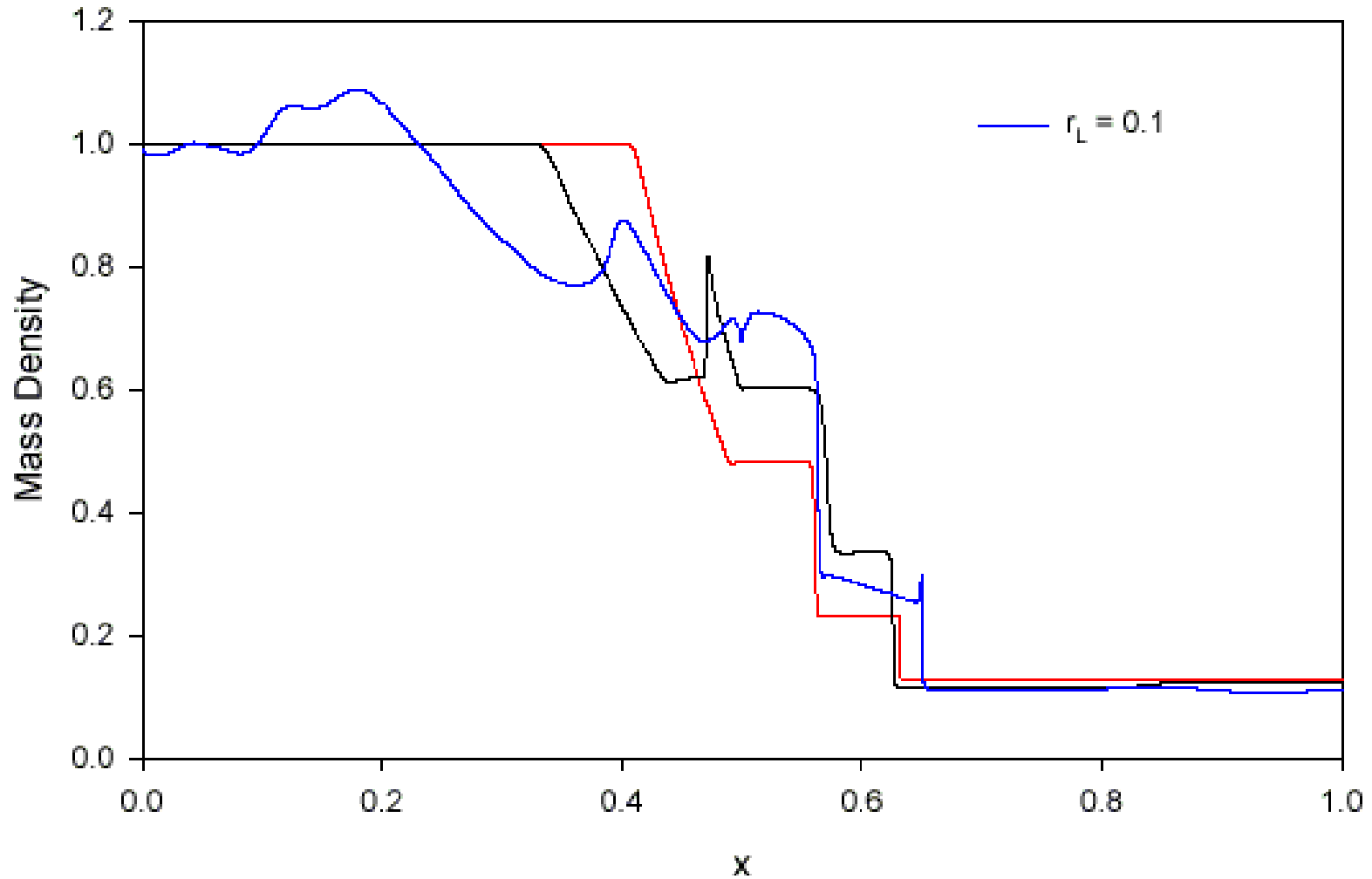
Application/comparison to electromagnetic plasma shock



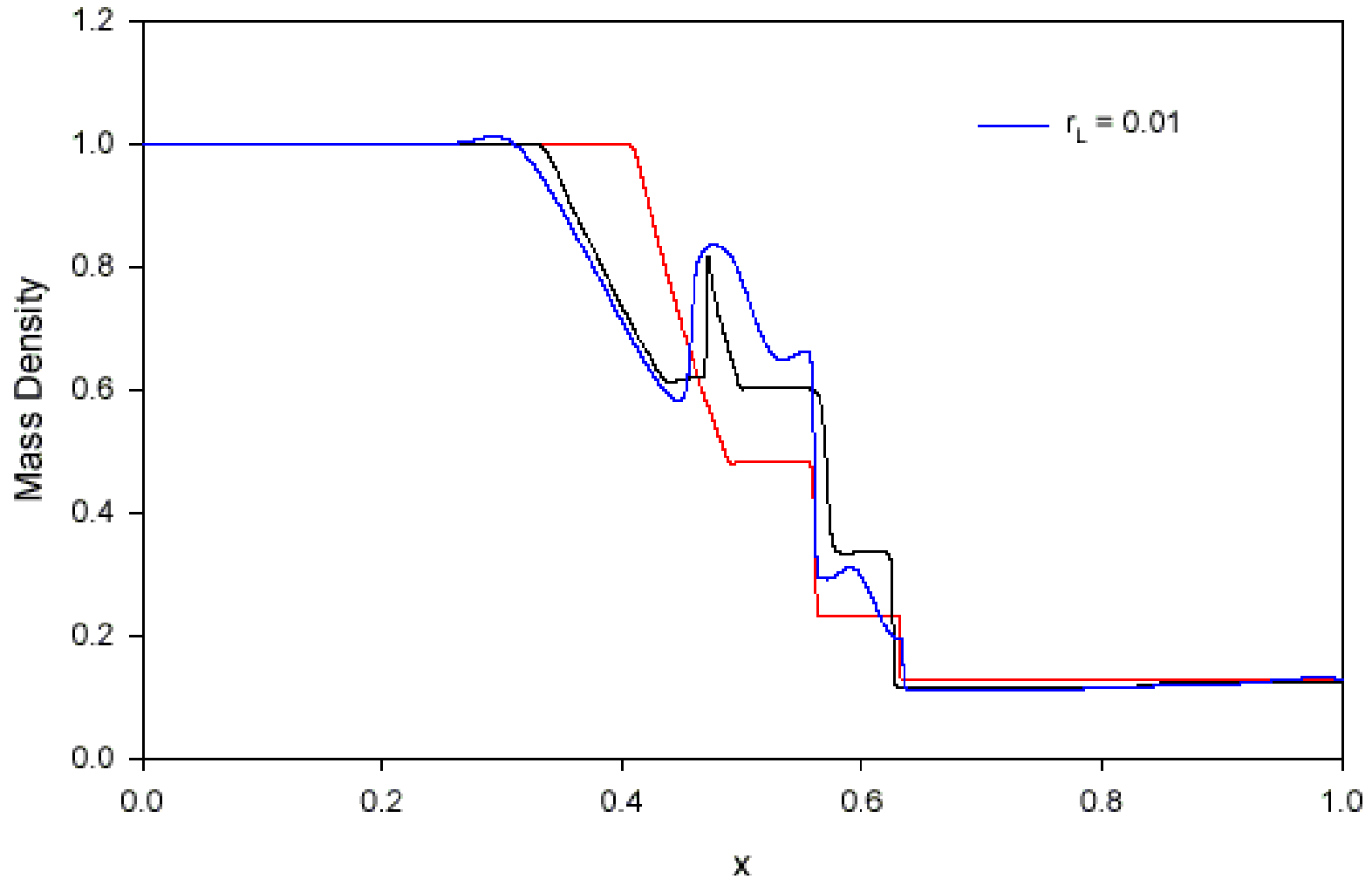
Application/comparison to electromagnetic plasma shock



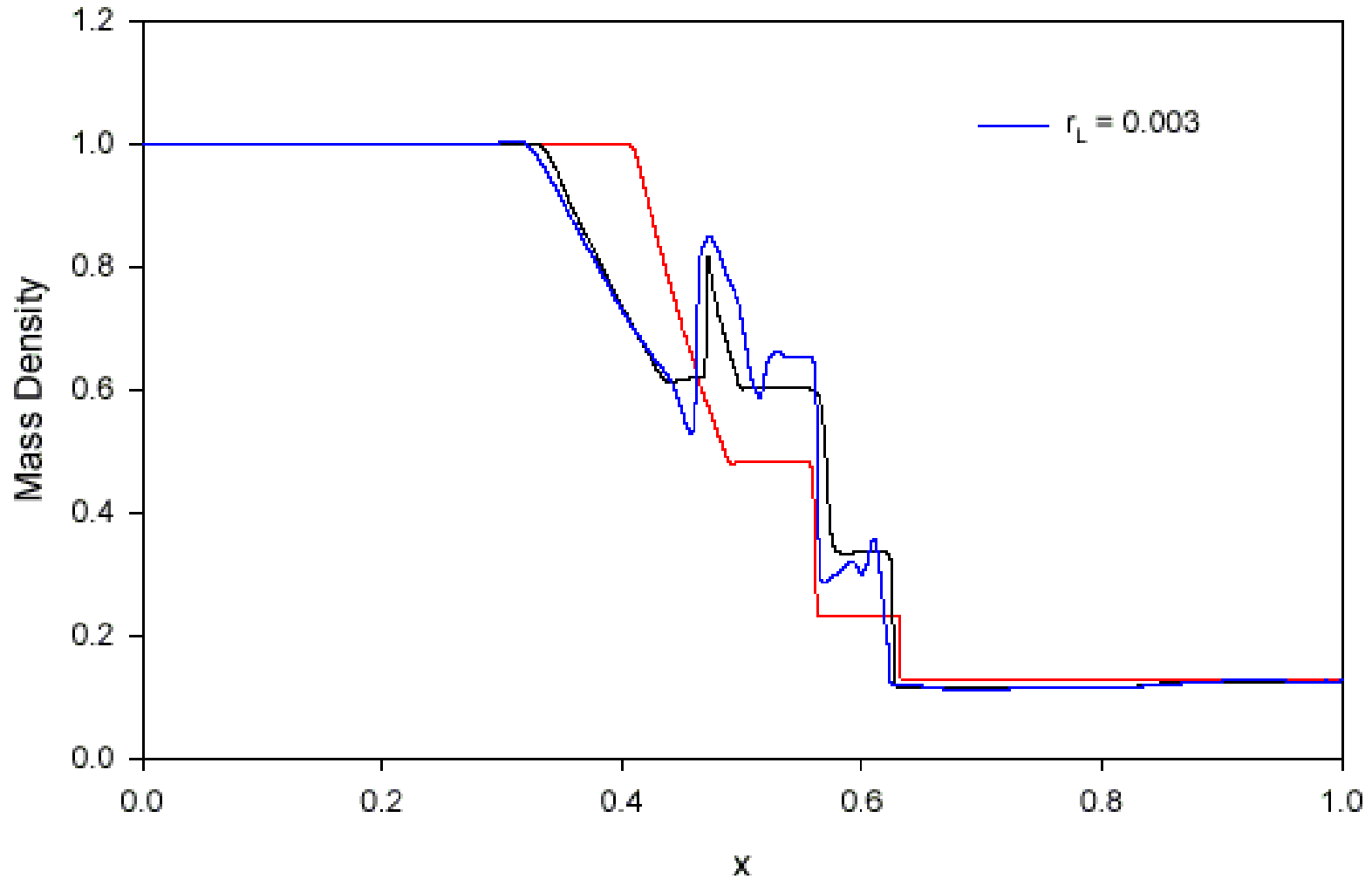
Application/comparison to electromagnetic plasma shock



Application/comparison to electromagnetic plasma shock



Application/comparison to electromagnetic plasma shock



Fast wave analysis in the electromagnetic plasma shock

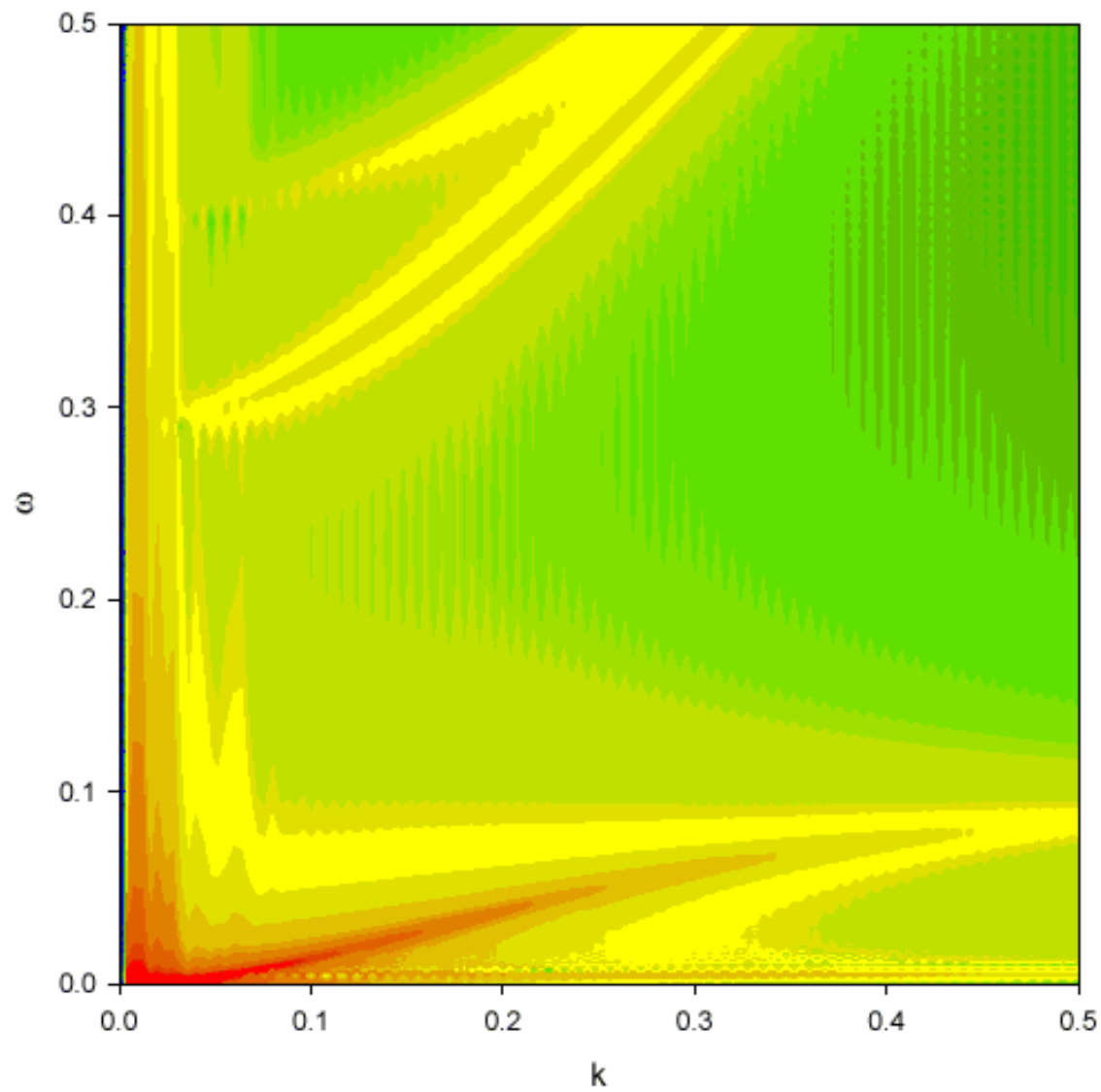
The wave vector is perpendicular to the discontinuity and parallel to the longitudinal magnetic field, $\mathbf{k} \parallel \mathbf{B}$.

The plasma dispersion relation for this case yields the left and right circularly polarized waves (L mode and R mode), in addition to the slower Alfvén waves.

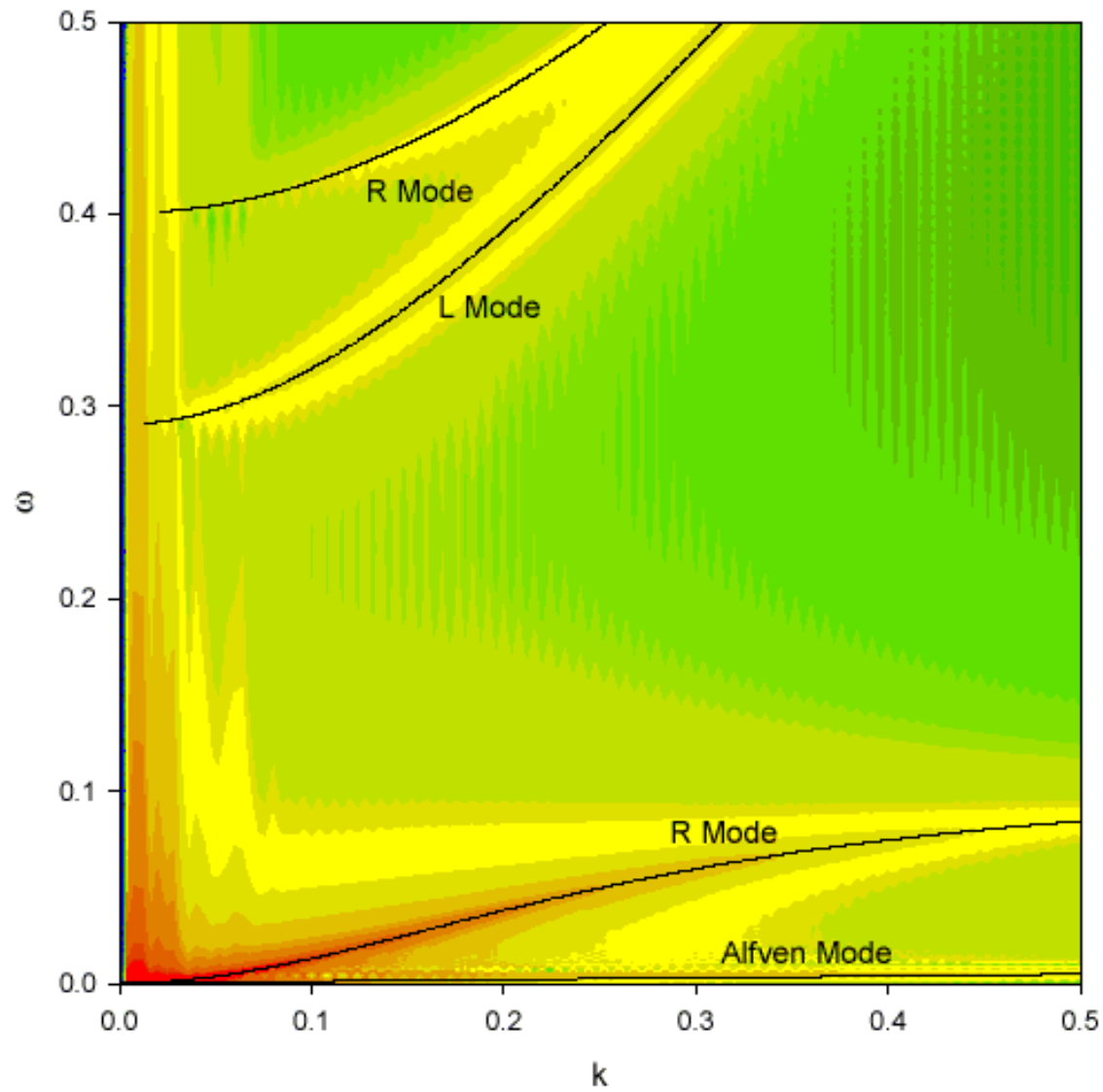
$$\frac{c^2 k^2}{\omega^2} = 1 - \frac{\omega_{pe}^2}{\omega(\omega \pm \omega_{ce})}$$

The low frequency portion of the lower branch of the R mode is the whistler wave.

Application/comparison to electromagnetic plasma shock



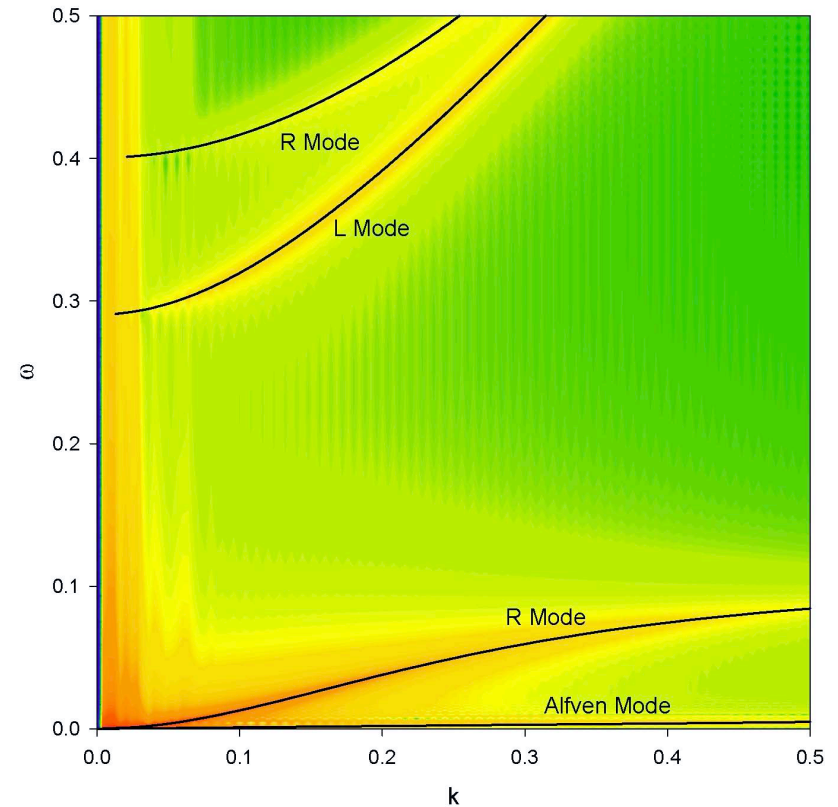
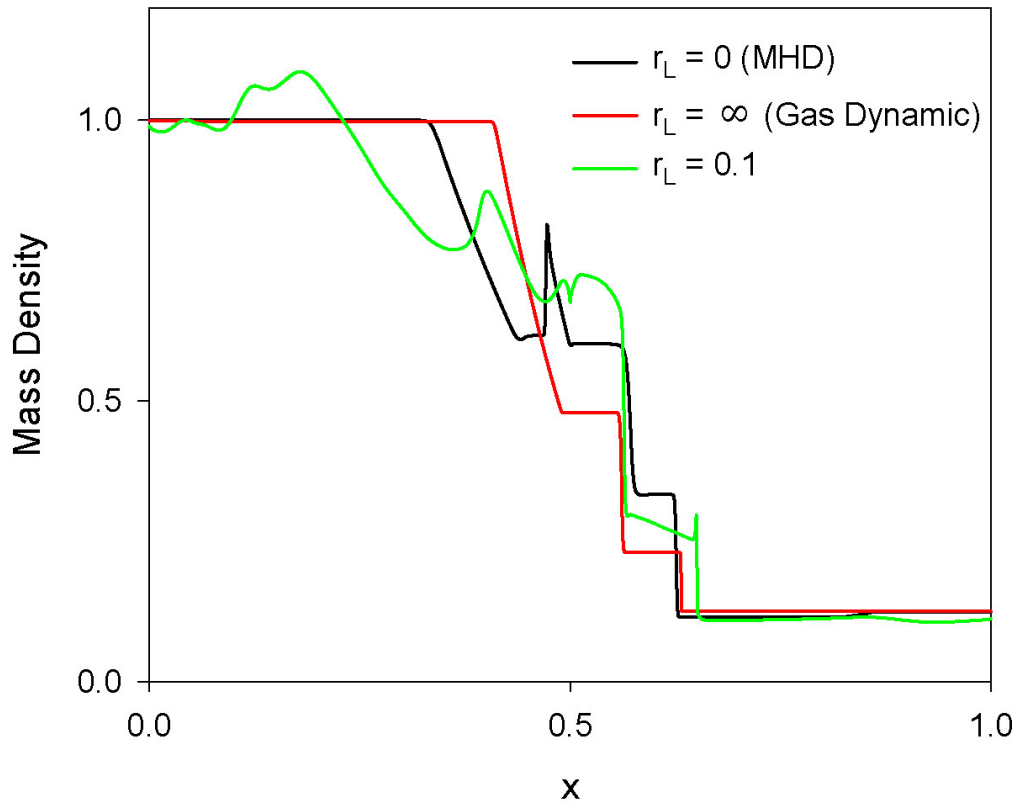
Application/comparison to electromagnetic plasma shock



Two-fluid plasma model captures expected waves*

Two-fluid plasma model spans the physical space beyond MHD. Physical scales and speeds are fundamental to the model: r_L , λ_D , c_{se} , c_{si} , c

The algorithm captures expected behavior in the limits: MHD ($r_L = 0$, $\lambda_D = 0$, $c = \infty$) or neutral gas ($r_L = \infty$, $\lambda_D = \infty$). Electron effects \rightarrow plasma waves.



Motivation for higher order accuracy

As mentioned earlier, a motivation for high order accuracy is the unsplit coupling of the hyperbolic fluxes and the source terms.

This is demonstrated by the propagation of electrostatic ion cyclotron waves and by equilibrium calculations.

The electrostatic ion cyclotron wave is a dispersive wave that results from adding a source term to the Euler equations. The momentum equation becomes

$$\rho \left(\frac{\partial \mathbf{u}}{\partial t} + u_x \frac{\partial \mathbf{u}}{\partial x} \right) + \frac{\partial p}{\partial x} = \rho \omega_c \frac{\mathbf{u} \times \mathbf{B}}{|B|}$$

This problem has an analytical solution of

$$u_x(x, t) = - \sum_{n=0}^{\infty} \frac{u^0}{2n+1} \sin(k_n x + \omega_n t)$$

where $\omega_n^2 = k_n^2 c_s^2 + \omega_c^2$.

DG improves accuracy for equivalent resolution.*

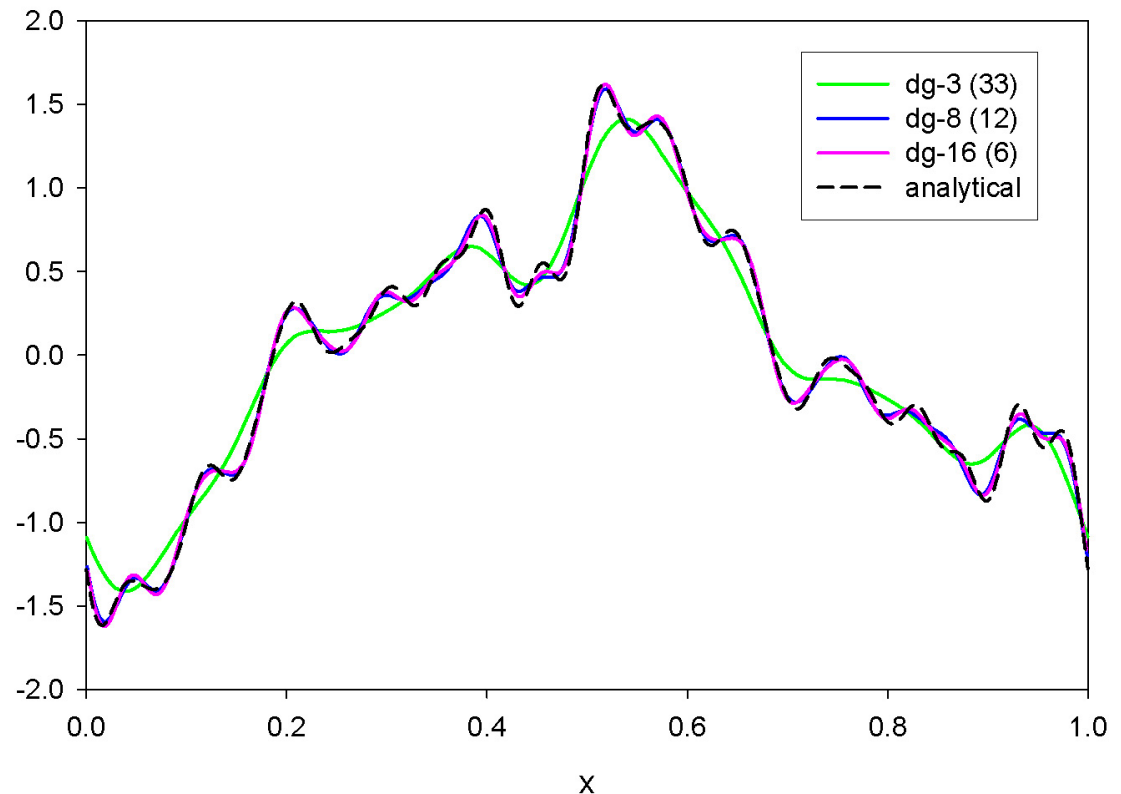
High-order, discontinuous Galerkin accurately captures the detailed spatial structure of plasma dynamics without large computational grids.

DG solutions are compared to second-order wave propagation solutions for electrostatic ion cyclotron waves (dispersive waves).

$$\omega_n^2 = k_n^2 c_s^2 + \omega_c^2$$

The effective resolution (defined as the number of unknowns) is held approx. constant. \Rightarrow

The benefit of using high-order is evident.



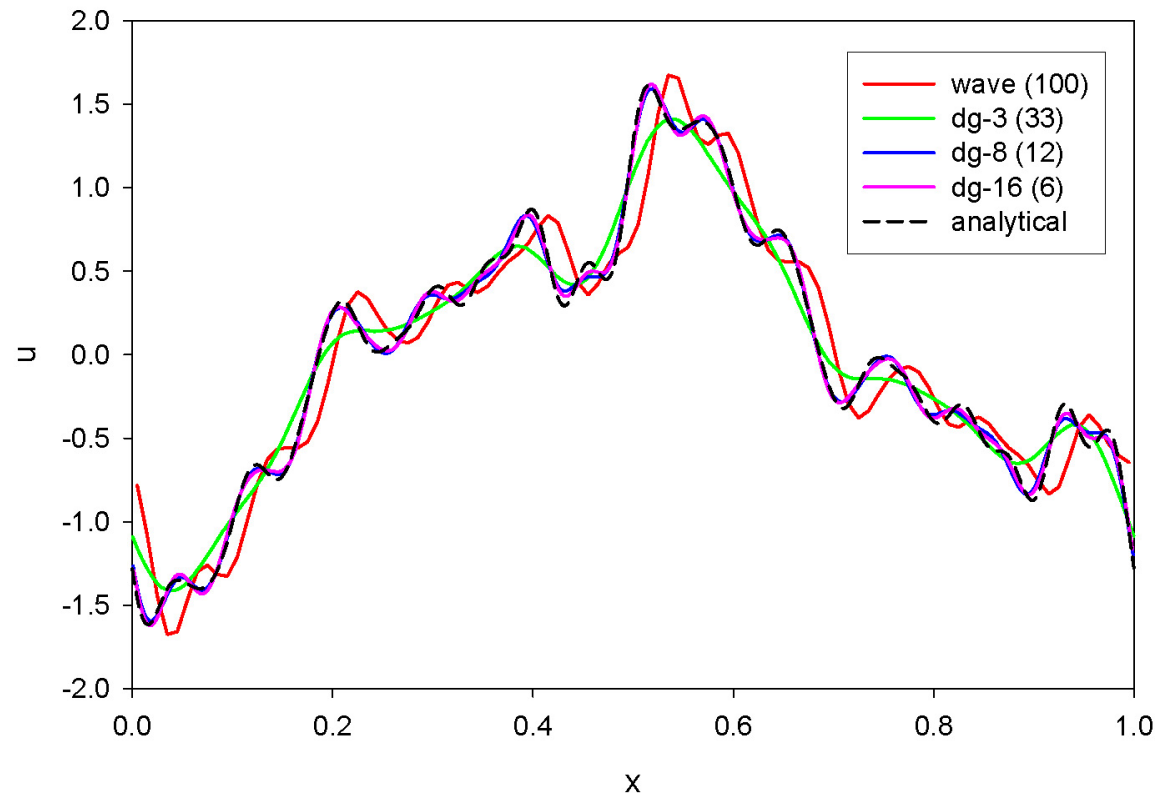
DG improves accuracy for equivalent resolution.*

High-order, discontinuous Galerkin accurately captures the detailed spatial structure of plasma dynamics without large computational grids.

DG solutions are compared to second-order wave propagation solutions for electrostatic ion cyclotron waves (dispersive waves).

$$\omega_n^2 = k_n^2 c_s^2 + \omega_c^2$$

The wave propagation method introduces a phase shift for the same effective resolution.



High order is important for preserving anisotropies*

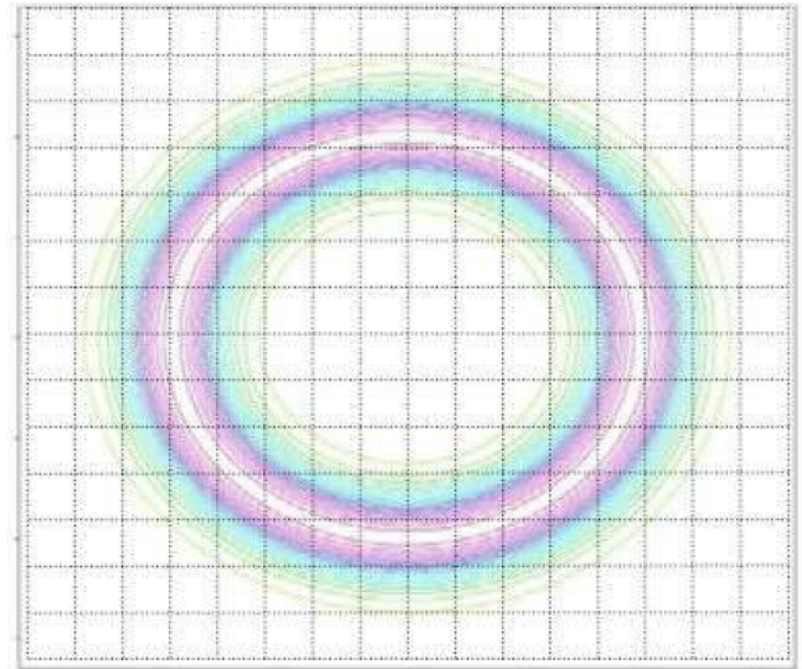
Plasmas are often strongly magnetized which produces strongly anisotropic transport properties. One example is thermal conductivity which can have parallel to perpendicular conductivities of 10^6 .

We investigate the ability of a finite element method to solve the anisotropic heat conduction equation.

$$\frac{\partial T}{\partial t} + \nabla \cdot (-\mathbf{D} \cdot \nabla T) = 0$$

where $\mathbf{D} = \mathbf{D}_{\parallel}(x, y, z) + \mathbf{D}_{\perp}(x, y, z)$.

A 3D problem with $\mathbf{D}_{\parallel} = 1$ and $\mathbf{D}_{\perp} = 0$.
A Gaussian temperature profile is specified aligned with a toroidal magnetic field. An effective \mathbf{D}_{\perp} is measured from the numerical simulations.

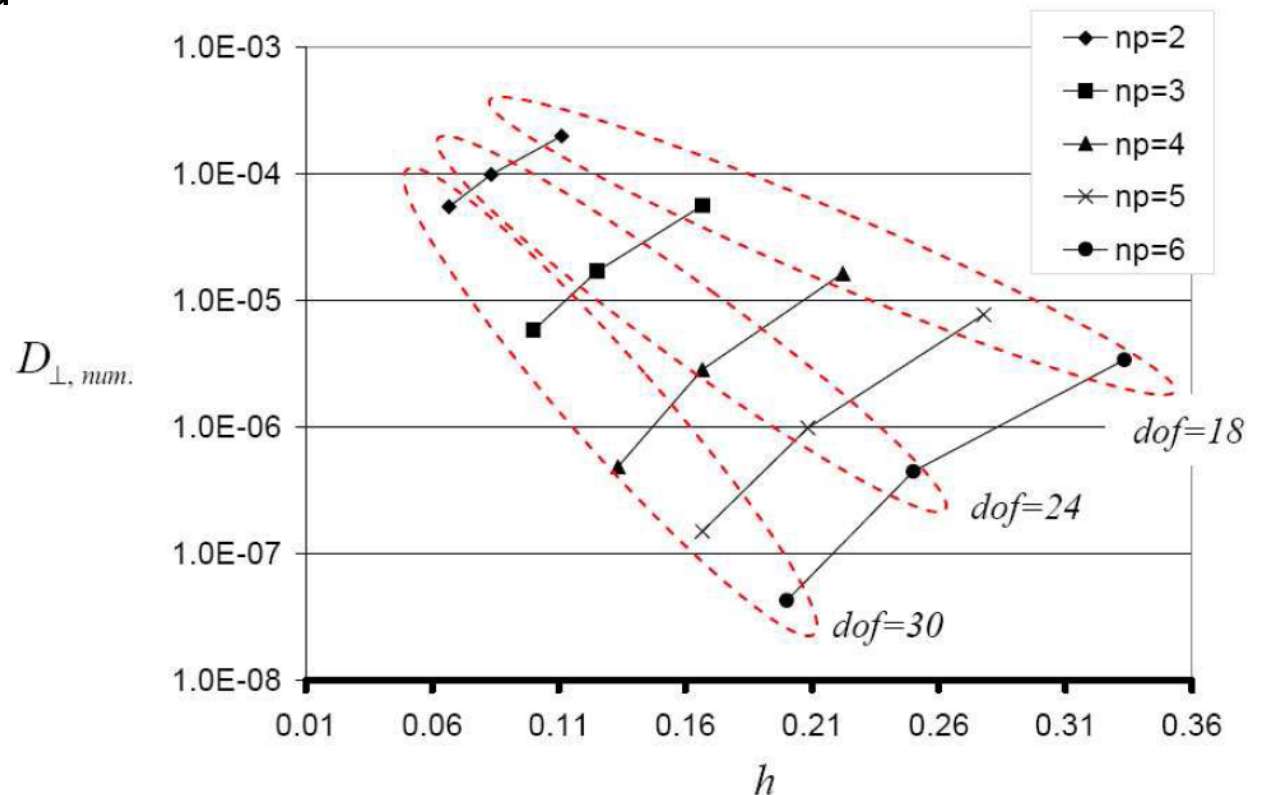


High order is important for preserving anisotropies*

The numerical results demonstrate the importance of high order spatial representation to capture the anisotropic heat conduction and the minimize the numerically generated \mathbf{D}_\perp .

Results show expected behavior for increased spatial resolution and for increased polynomial order.

Even for constant $dof = N_x np$, higher order is better able to preserve anisotropy.



Dynamics of the electromagnetic fields are modeled

Maxwell's equations govern the evolution of the electromagnetic fields.

The fields couple to the fluids through source terms.

$$\frac{\partial \mathbf{B}}{\partial t} + \nabla \times \mathbf{E} = 0$$

$$\frac{\partial \mathbf{E}}{\partial t} - c^2 \nabla \times \mathbf{B} = -\frac{1}{\epsilon_0} \sum_s \frac{\rho_s q_s}{m_s} \mathbf{u}_s$$

In addition to these time-dependent equations, two divergence equations (involutions) must also be satisfied.

$$\nabla \cdot \mathbf{B} = 0 \qquad \nabla \cdot \mathbf{E} = \frac{1}{\epsilon_0} \sum_s \frac{\rho_s q_s}{m_s}$$

Violation of these constraints leads to nonphysical effects – charge generation and parallel magnetic forces.

Divergence conditions can be enforced by purely hyperbolic formulation or with a mixed potential formulation.

Hyperbolic form provides uniform treatment of fields

The divergence constraints are transformed into hyperbolic equations and coupled to the dynamical equations (Faraday's and Ampere's laws).*

$$\begin{aligned}\frac{\partial \mathbf{B}}{\partial t} + \nabla \times \mathbf{E} + \gamma \nabla \psi &= 0 \\ \frac{\partial \mathbf{E}}{\partial t} - c^2 \nabla \times \mathbf{B} + \chi c^2 \nabla \phi &= -\frac{1}{\epsilon_0} \sum_s \frac{q_s \rho_s}{m_s} \mathbf{u}_s \\ \frac{\partial \phi}{\partial t} + \chi \nabla \cdot \mathbf{E} &= \frac{\chi}{\epsilon_0} \sum_s \frac{q_s \rho_s}{m_s} \\ \frac{\partial \psi}{\partial t} + \gamma c^2 \nabla \cdot \mathbf{B} &= 0\end{aligned}$$

Divergence error correction potentials ϕ and ψ “sweep” the divergence error out of the domain at speeds χ and γ which are greater than c .

Hyperbolic form provides uniform treatment of fields

The divergence constraints are transformed into hyperbolic equations and coupled to the dynamical equations (Faraday's and Ampere's laws).*

$$\begin{aligned}\frac{\partial \mathbf{B}}{\partial t} + \nabla \times \mathbf{E} + \gamma \nabla \psi &= 0 \\ \frac{\partial \mathbf{E}}{\partial t} - c^2 \nabla \times \mathbf{B} + \chi c^2 \nabla \phi &= -\frac{1}{\epsilon_0} \sum_s \frac{q_s \rho_s}{m_s} \mathbf{u}_s \\ \frac{\partial \phi}{\partial t} + \chi \nabla \cdot \mathbf{E} &= \frac{\chi}{\epsilon_0} \sum_s \frac{q_s \rho_s}{m_s} \\ \frac{\partial \psi}{\partial t} + \gamma c^2 \nabla \cdot \mathbf{B} &= 0\end{aligned}$$

Divergence error correction potentials ϕ and ψ “sweep” the divergence error out of the domain at speeds χ and γ which are greater than c .

Mixed potential formulation satisfies involutions

Another approach introduces potentials to transform Maxwell's equations to automatically satisfy the divergence constraints.

$$\mathbf{E} = -\nabla\Phi - \frac{\partial\mathbf{A}}{\partial t} \quad \text{and} \quad \mathbf{B} = \nabla \times \mathbf{A}$$

Substitution into Maxwell's equations results in 2nd order equations for the potentials. A gauge condition must also be selected for $\nabla \cdot \mathbf{A}$. Common choices are either the Coulomb gauge or ...

$$\nabla \cdot \mathbf{A} = 0$$

which gives

$$\nabla^2\Phi = -\frac{1}{\epsilon_0} \sum_s \frac{q_s \rho_s}{m_s}$$
$$\frac{\partial^2 \mathbf{A}}{\partial t^2} - c^2 \nabla^2 \mathbf{A} = \frac{1}{\epsilon_0} \sum_s \frac{q_s \rho_s}{m_s} \mathbf{u}_s - \nabla \left(\frac{\partial \Phi}{\partial t} \right)$$

Mixed potential formulation satisfies involutions

Another approach introduces potentials to transform Maxwell's equations to automatically satisfy the divergence constraints.

$$\mathbf{E} = -\nabla\Phi - \frac{\partial\mathbf{A}}{\partial t} \quad \text{and} \quad \mathbf{B} = \nabla \times \mathbf{A}$$

Substitution into Maxwell's equations results in 2nd order equations for the potentials. A gauge condition must also be selected for $\nabla \cdot \mathbf{A}$. Common choices are either the Coulomb gauge or the Lorenz gauge.

$$\nabla \cdot \mathbf{A} = -\frac{1}{c^2} \frac{\partial\Phi}{\partial t}$$

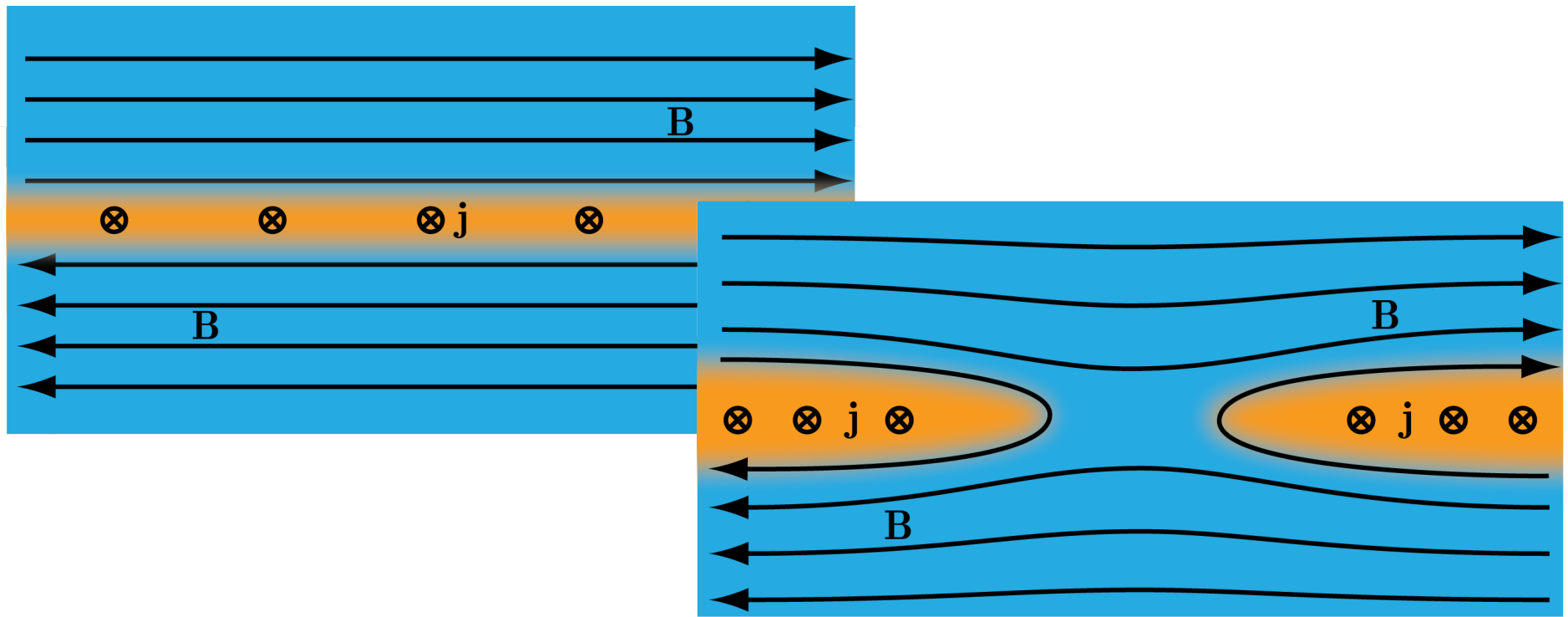
which gives

$$\frac{\partial^2\Phi}{\partial t^2} - c^2\nabla^2\Phi = \frac{c^2}{\epsilon_0} \sum_s \frac{q_s\rho_s}{m_s}$$
$$\frac{\partial^2\mathbf{A}}{\partial t^2} - c^2\nabla^2\mathbf{A} = \frac{1}{\epsilon_0} \sum_s \frac{q_s\rho_s}{m_s} \mathbf{u}_s$$

Improved electromagnetic models are benchmarked

Current coalesces and magnetic flux reconnects through the current layer without requiring collisional effects → GEM reconnection challenge.*

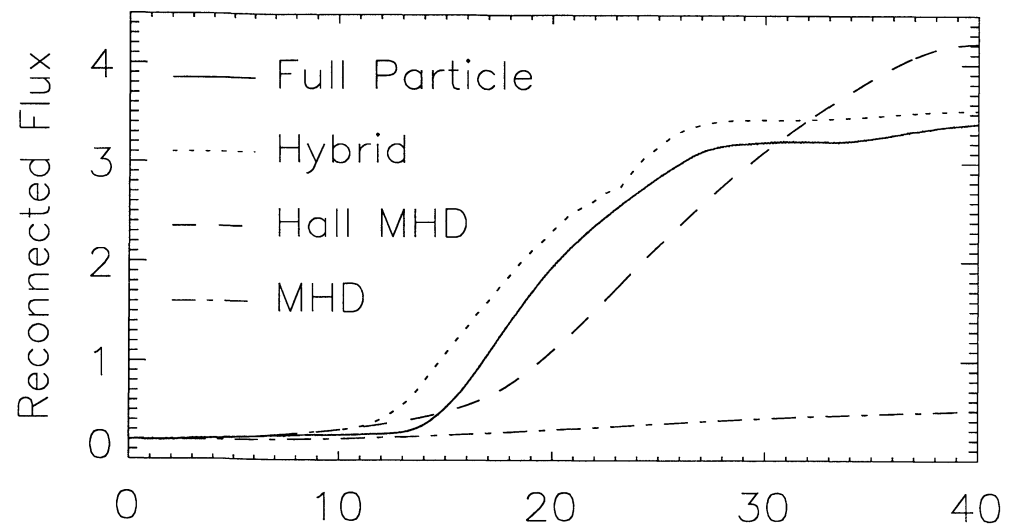
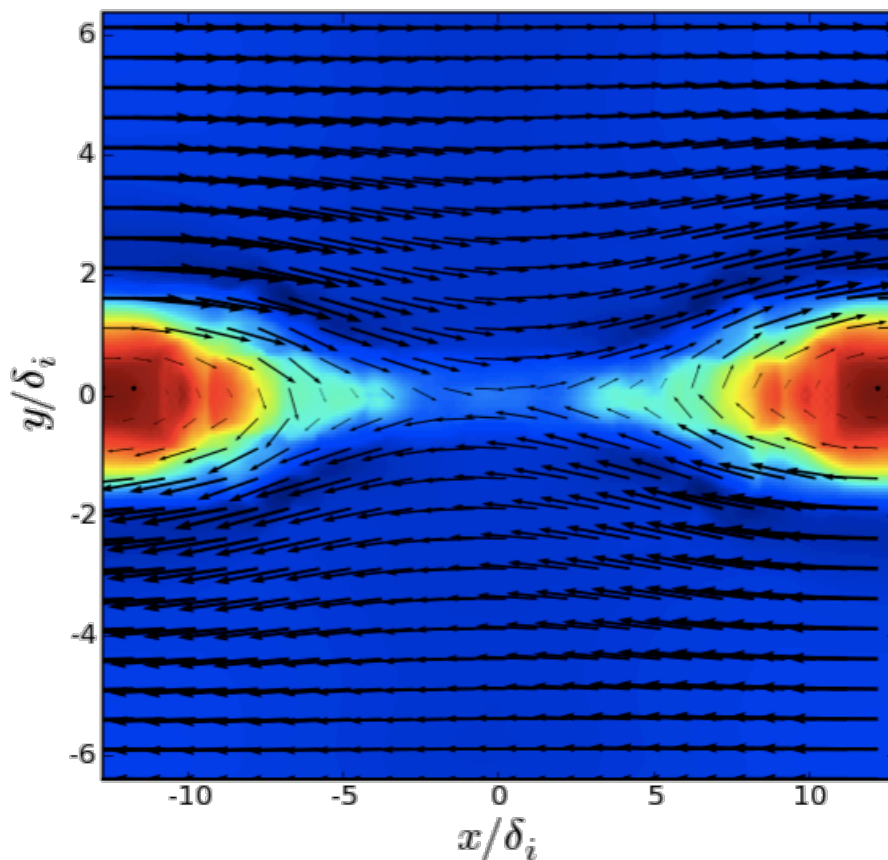
Because the reconnection process involves magnetic field lines tearing and reconnecting, the problem is susceptible to generating non-solenoidal magnetic fields, $\nabla \cdot \mathbf{B} \neq 0$ (divergence errors).



Collisionless magnetic reconnection plasma benchmark

Current coalesces and magnetic flux reconnects through the current layer without requiring collisional effects → GEM reconnection challenge.*

The problem has been solved by several different plasma models.

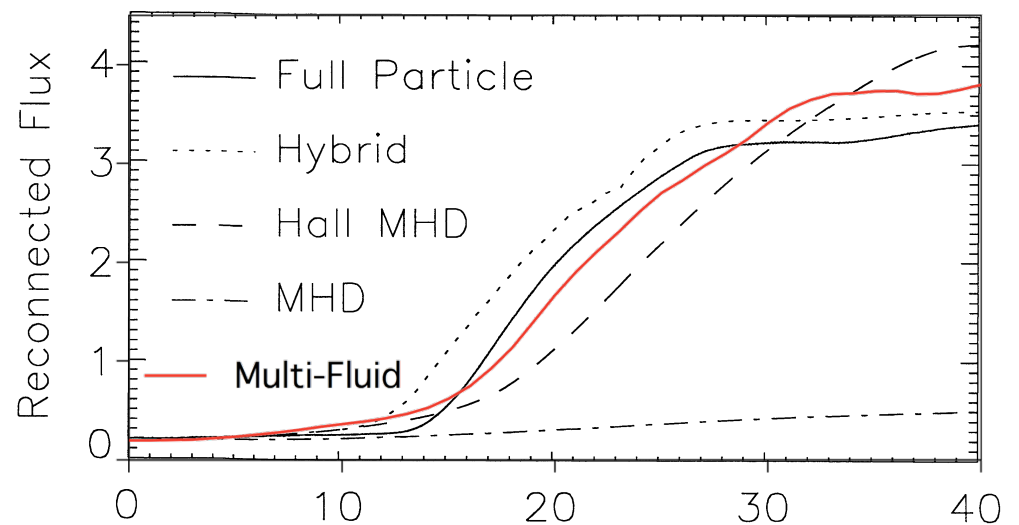
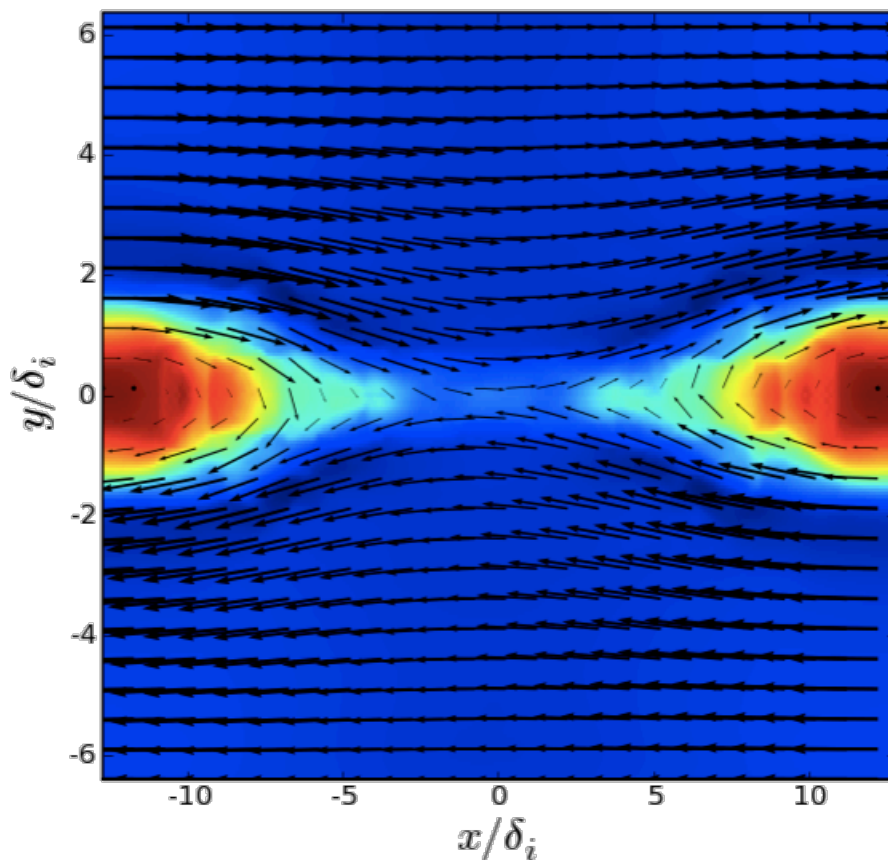


MHD model lacks sufficient physical completeness for the problem and is unable to model collisionless reconnection.

Collisionless magnetic reconnection plasma benchmark

Current coalesces and magnetic flux reconnects through the current layer without requiring collisional effects → GEM reconnection challenge.*

The problem has been solved by several different plasma models.

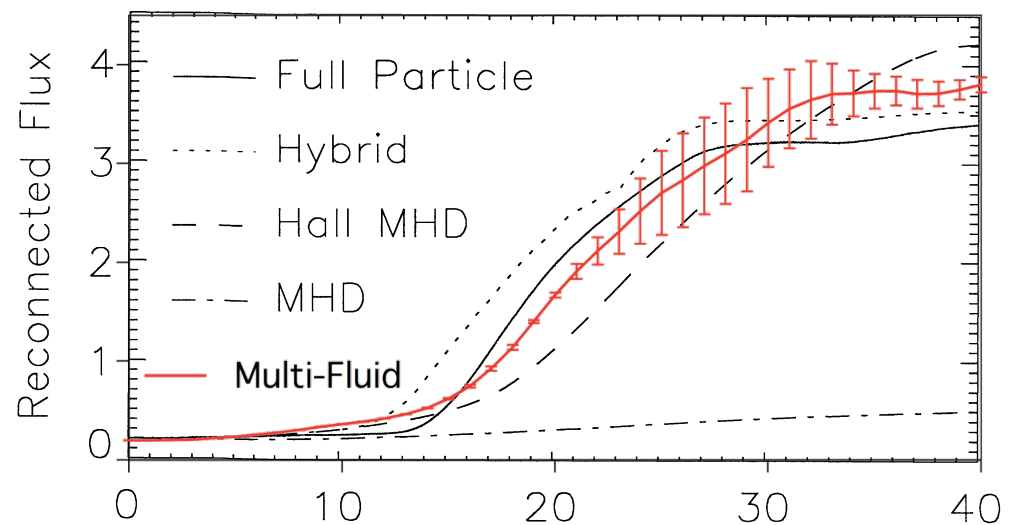
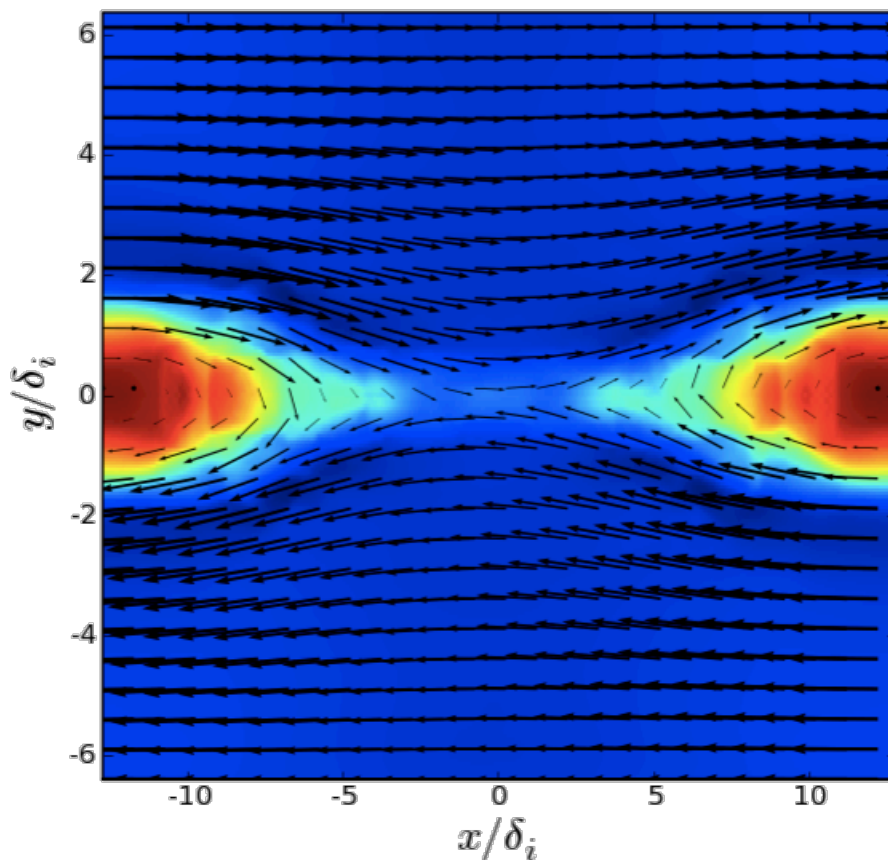


Solutions with the multi-fluid model agree with the published results.^

Collisionless magnetic reconnection plasma benchmark

Current coalesces and magnetic flux reconnects through the current layer without requiring collisional effects → GEM reconnection challenge.

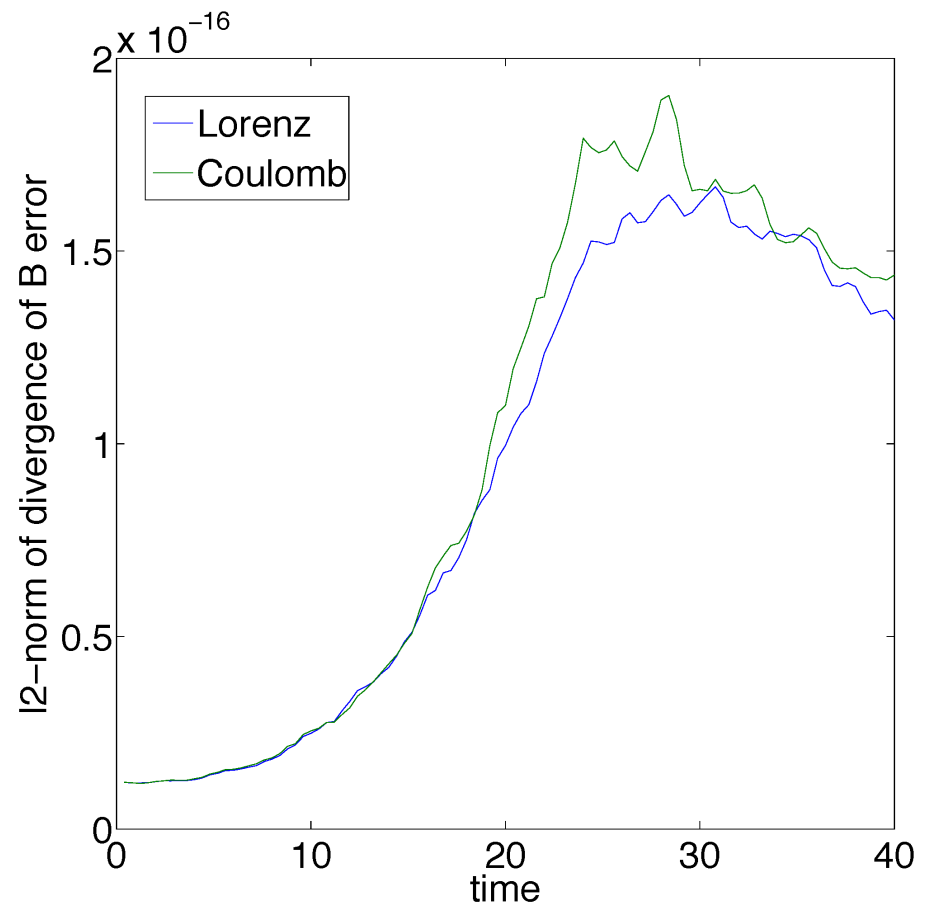
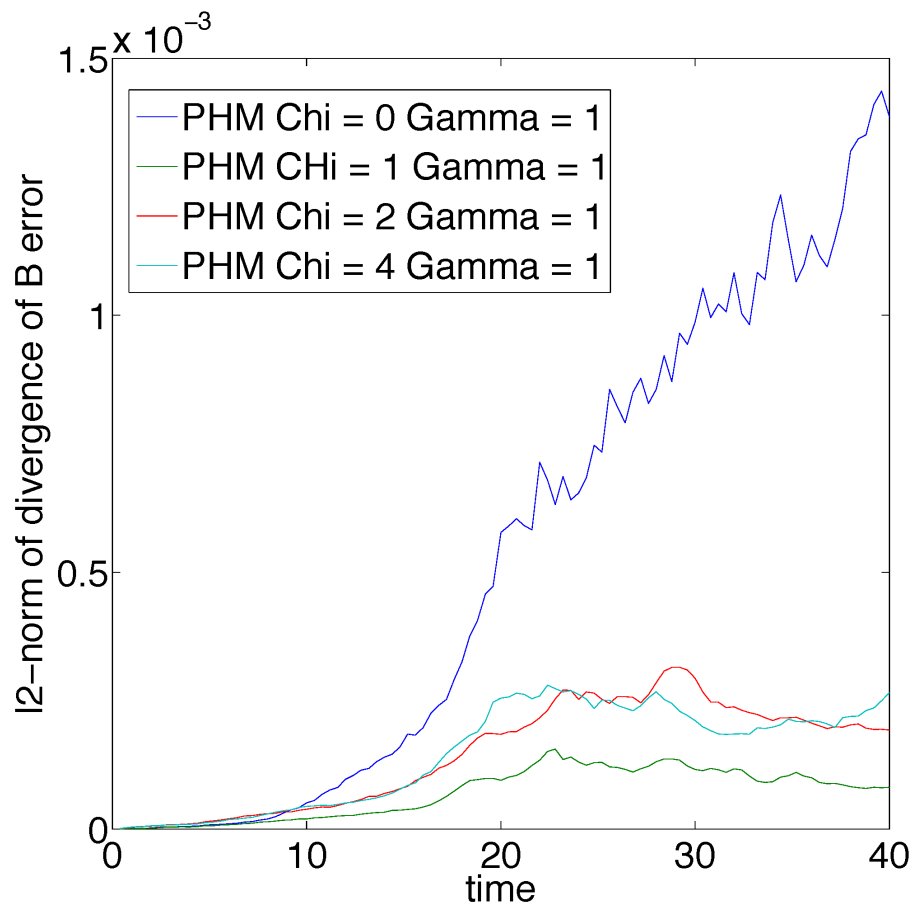
The problem has been solved by several different plasma models.



Uncertainty quantification analysis of the multi-fluid plasma model has provided a more rigorous validation test of agreement.

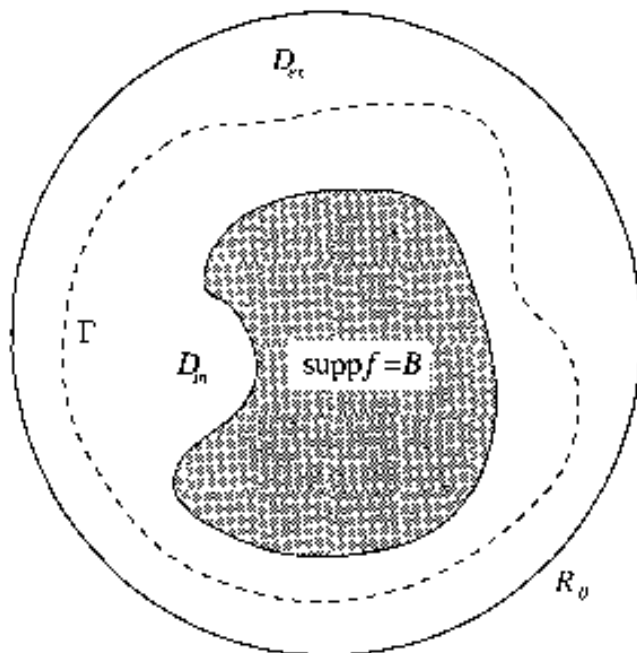
Improved electromagnetic models are benchmarked

The divergence error is significantly reduced with the perfectly hyperbolic formulation. The mixed potential formulation reduces the error to machine precision, at greater computational expense.

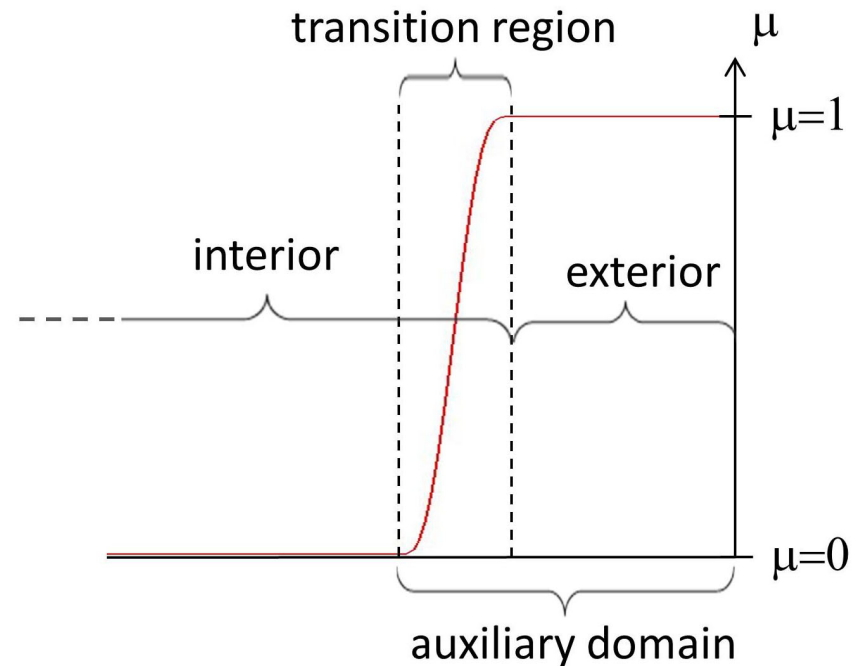


Non-local boundary conditions to absorb waves

Since the multi-fluid plasma model has fast light waves and slower ion acoustic waves, non-physical reflections of fast waves at open boundaries are likely. Non-local boundary conditions use a lacuna-based methods that match an interface condition.* The matching is provided by auxiliary source.



The additional domain is shown in 1D.



Non-local boundary conditions to absorb waves*

The governing equation in the interior domain is expressed as

$$\frac{\partial q}{\partial t} + \nabla \cdot \mathbf{F} = S,$$

while in the auxiliary domain the governing equation is defined as

$$\frac{\partial w}{\partial t} + \nabla \cdot \mathbf{F}(w) = S(w) + \Omega(q),$$

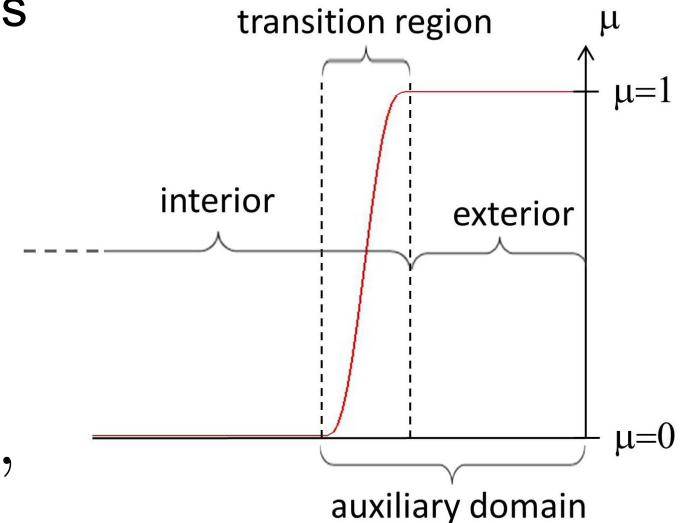
with the requirement that $w = q\mu(x)$ gives the “near-boundary source” as

$$\Omega(q) = \nabla \cdot \mathbf{F}(\mu q) - S(\mu q) - \mu \nabla \cdot \mathbf{F}(q) + \mu S(q).$$

The boundary condition for the interior solution is set such that

$$q|_{interface}^- = w|_{interface}^+$$

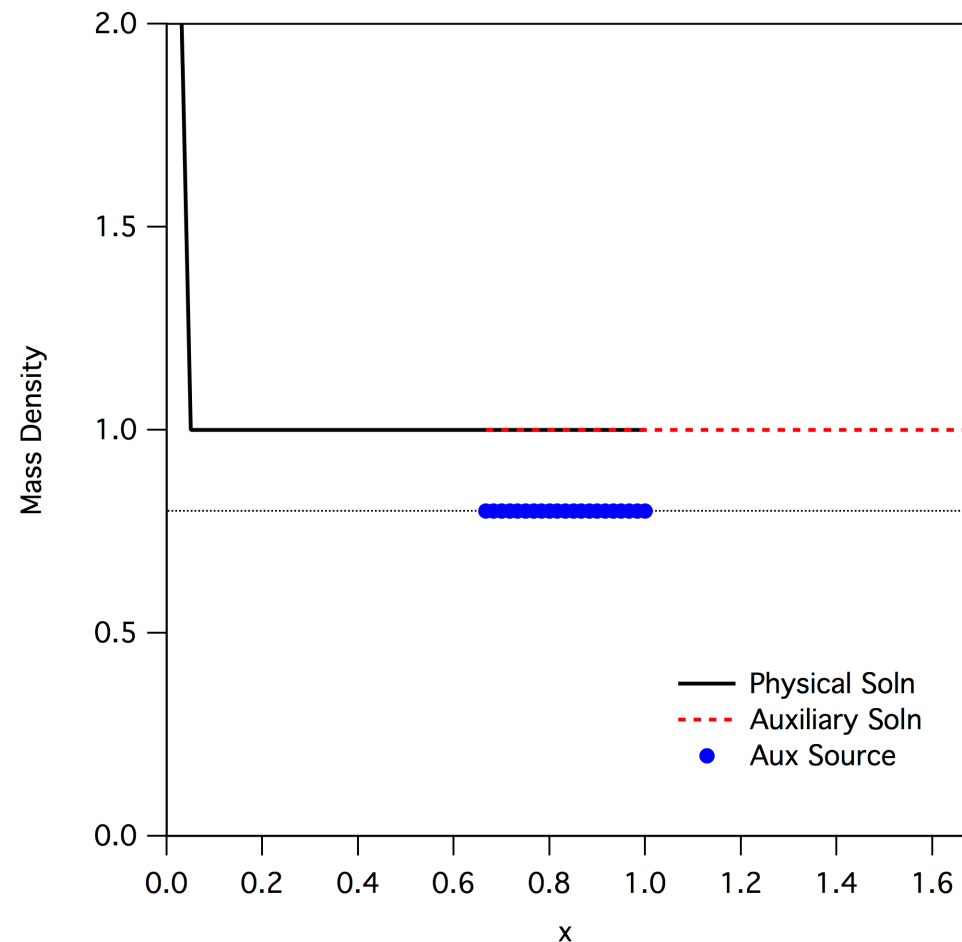
The auxiliary solution is periodically re-integrated to damp the solution before it reflects and contaminates the solution at the interface.



Non-local boundary conditions demonstrated in 1D

Other methods have been used to reduce reflections, e.g. Riemann methods, PML. However, they are limited to normal incidence, purely hyperbolic, or problem-specific frequencies. The lacuna-based methods offer more versatility.

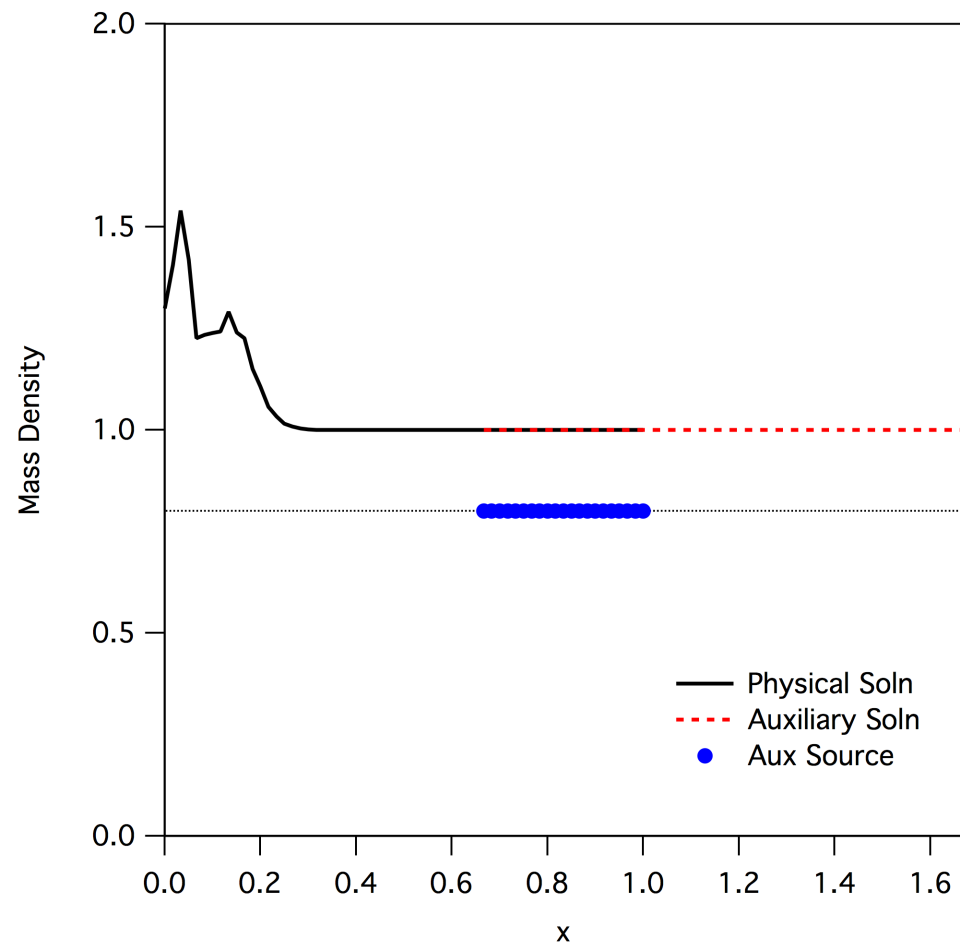
To demonstrate the effectiveness of the non-local boundary conditions, a 1D pulse is modeled using the Euler equations with thermal heat conduction.



Non-local boundary conditions demonstrated in 1D

Other methods have been used to reduce reflections, e.g. Riemann methods, PML. However, they are limited to normal incidence, purely hyperbolic, or problem-specific frequencies. The lacuna-based methods offer more versatility.

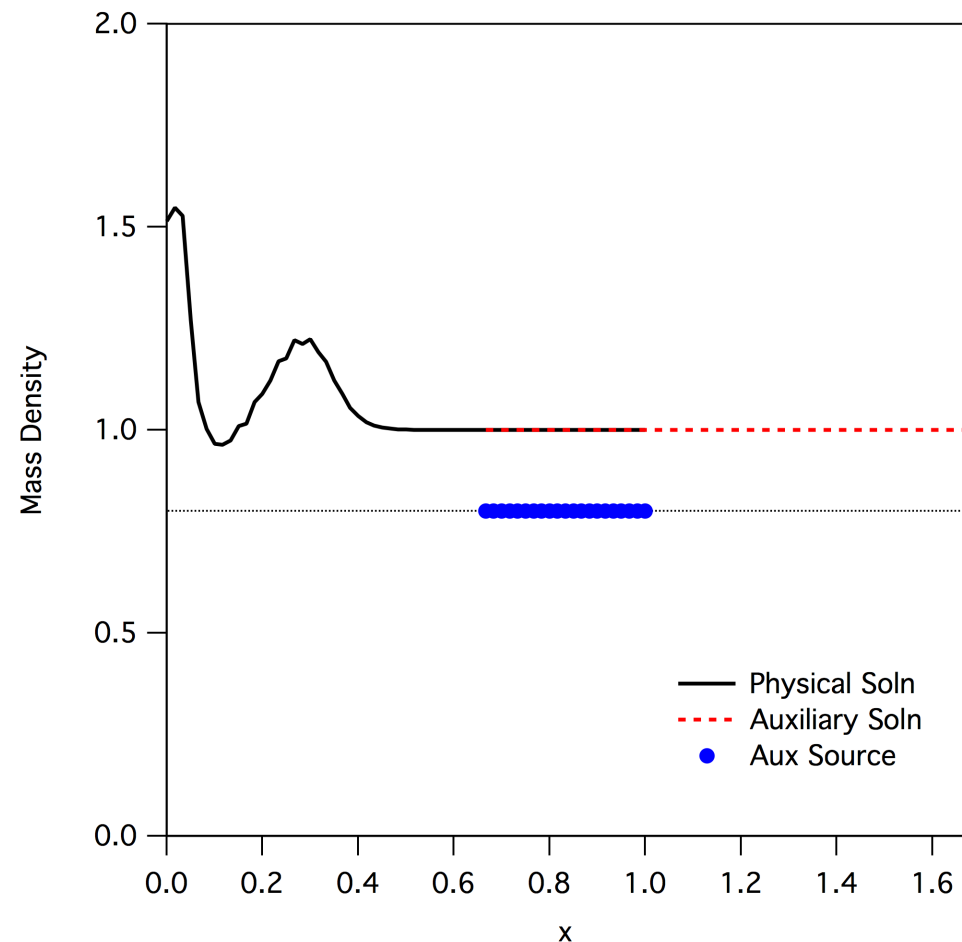
To demonstrate the effectiveness of the non-local boundary conditions, a 1D pulse is modeled using the Euler equations with thermal heat conduction.



Non-local boundary conditions demonstrated in 1D

Other methods have been used to reduce reflections, e.g. Riemann methods, PML. However, they are limited to normal incidence, purely hyperbolic, or problem-specific frequencies. The lacuna-based methods offer more versatility.

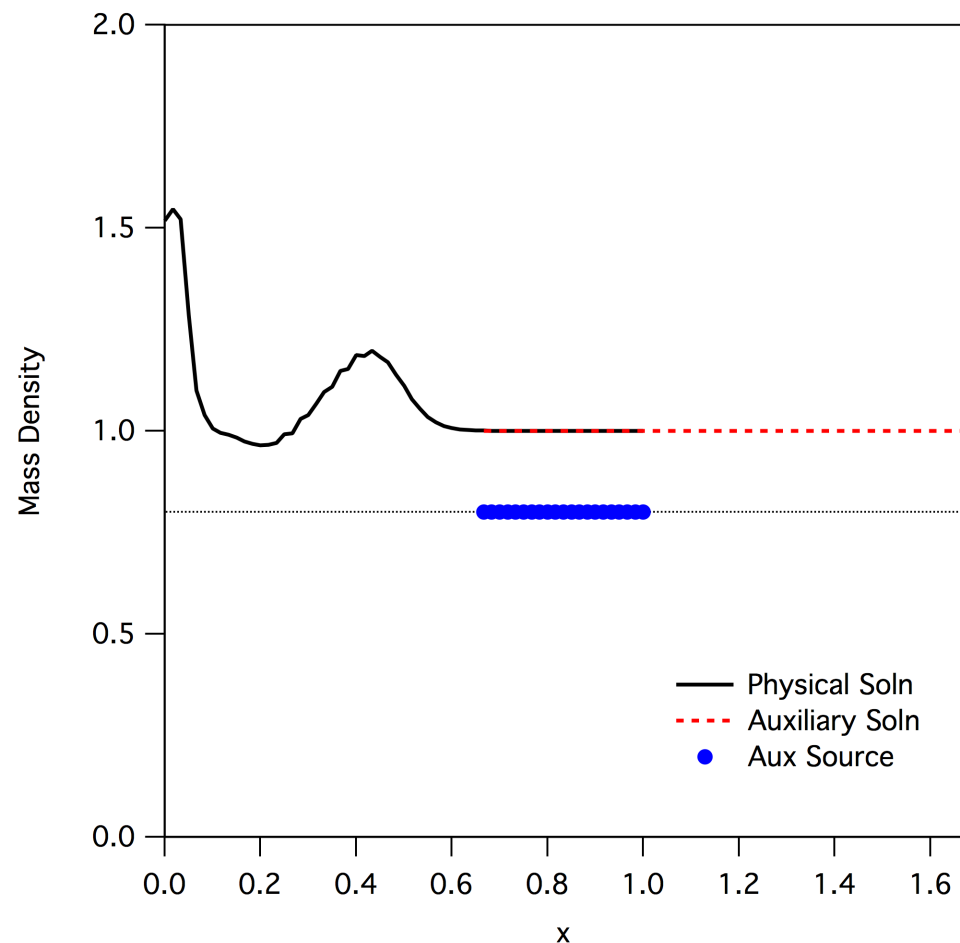
To demonstrate the effectiveness of the non-local boundary conditions, a 1D pulse is modeled using the Euler equations with thermal heat conduction.



Non-local boundary conditions demonstrated in 1D

Other methods have been used to reduce reflections, e.g. Riemann methods, PML. However, they are limited to normal incidence, purely hyperbolic, or problem-specific frequencies. The lacuna-based methods offer more versatility.

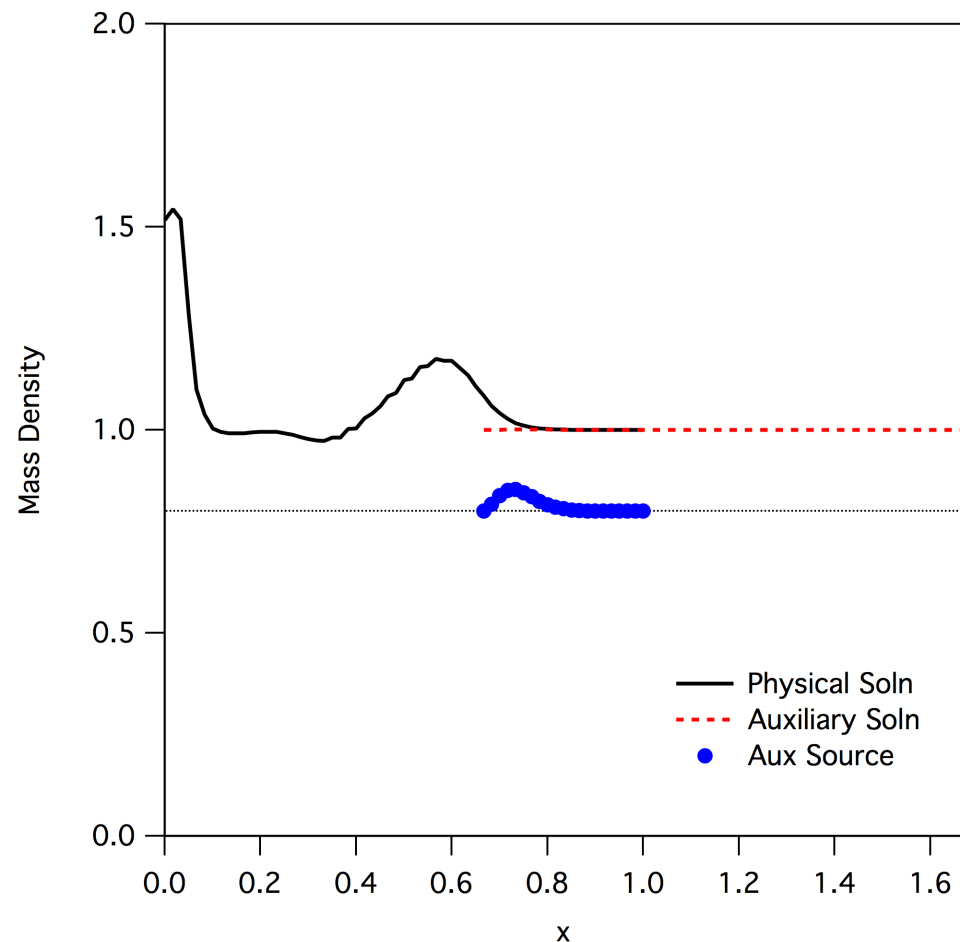
To demonstrate the effectiveness of the non-local boundary conditions, a 1D pulse is modeled using the Euler equations with thermal heat conduction.



Non-local boundary conditions demonstrated in 1D

Other methods have been used to reduce reflections, e.g. Riemann methods, PML. However, they are limited to normal incidence, purely hyperbolic, or problem-specific frequencies. The lacuna-based methods offer more versatility.

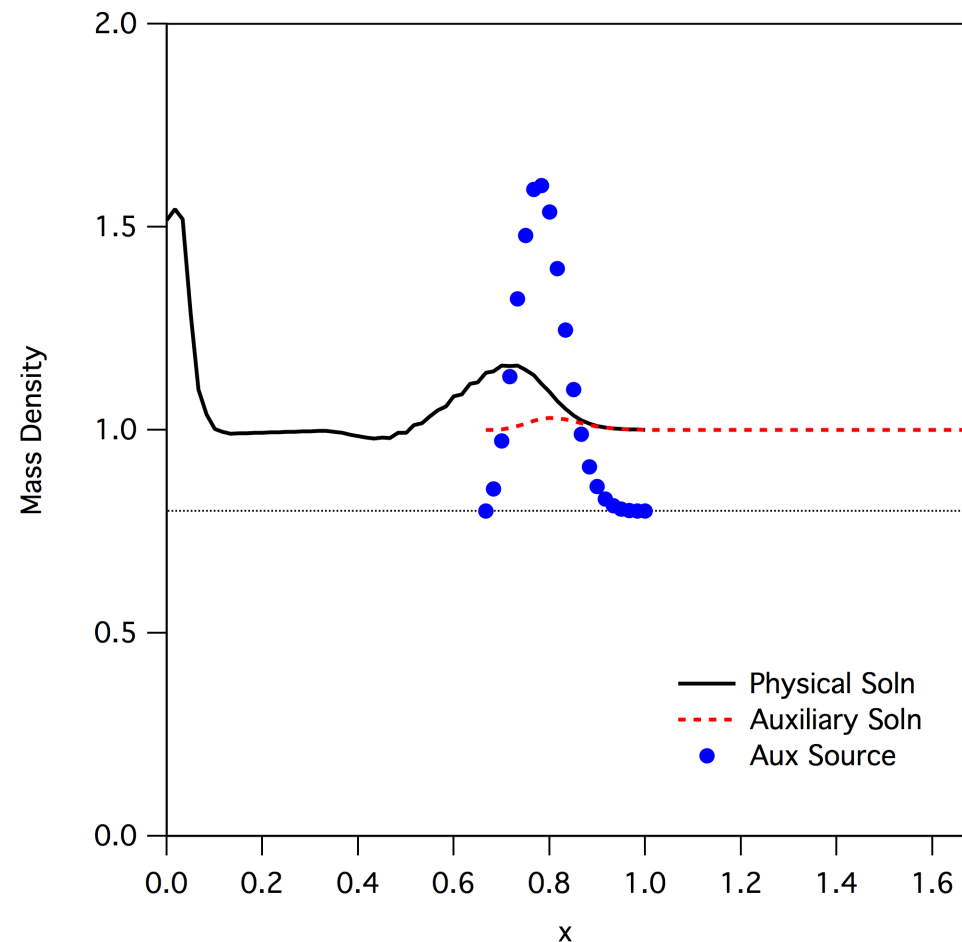
To demonstrate the effectiveness of the non-local boundary conditions, a 1D pulse is modeled using the Euler equations with thermal heat conduction.



Non-local boundary conditions demonstrated in 1D

Other methods have been used to reduce reflections, e.g. Riemann methods, PML. However, they are limited to normal incidence, purely hyperbolic, or problem-specific frequencies. The lacuna-based methods offer more versatility.

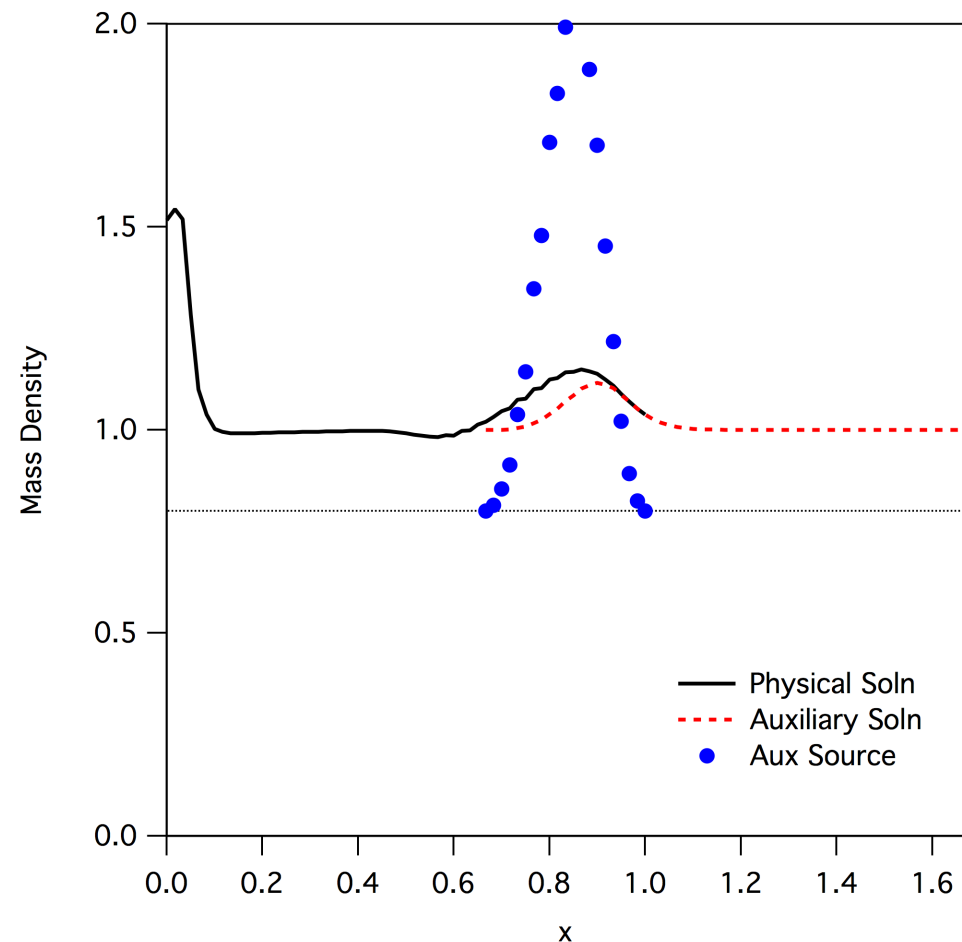
To demonstrate the effectiveness of the non-local boundary conditions, a 1D pulse is modeled using the Euler equations with thermal heat conduction.



Non-local boundary conditions demonstrated in 1D

Other methods have been used to reduce reflections, e.g. Riemann methods, PML. However, they are limited to normal incidence, purely hyperbolic, or problem-specific frequencies. The lacuna-based methods offer more versatility.

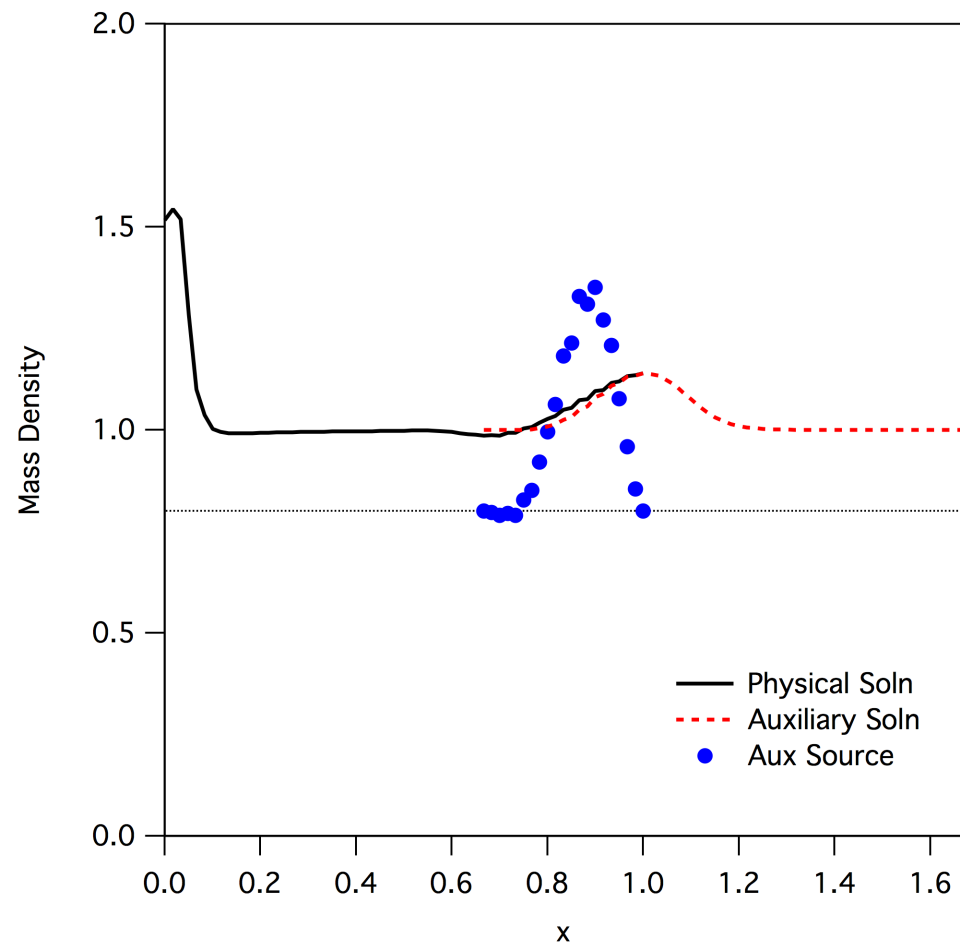
To demonstrate the effectiveness of the non-local boundary conditions, a 1D pulse is modeled using the Euler equations with thermal heat conduction.



Non-local boundary conditions demonstrated in 1D

Other methods have been used to reduce reflections, e.g. Riemann methods, PML. However, they are limited to normal incidence, purely hyperbolic, or problem-specific frequencies. The lacuna-based methods offer more versatility.

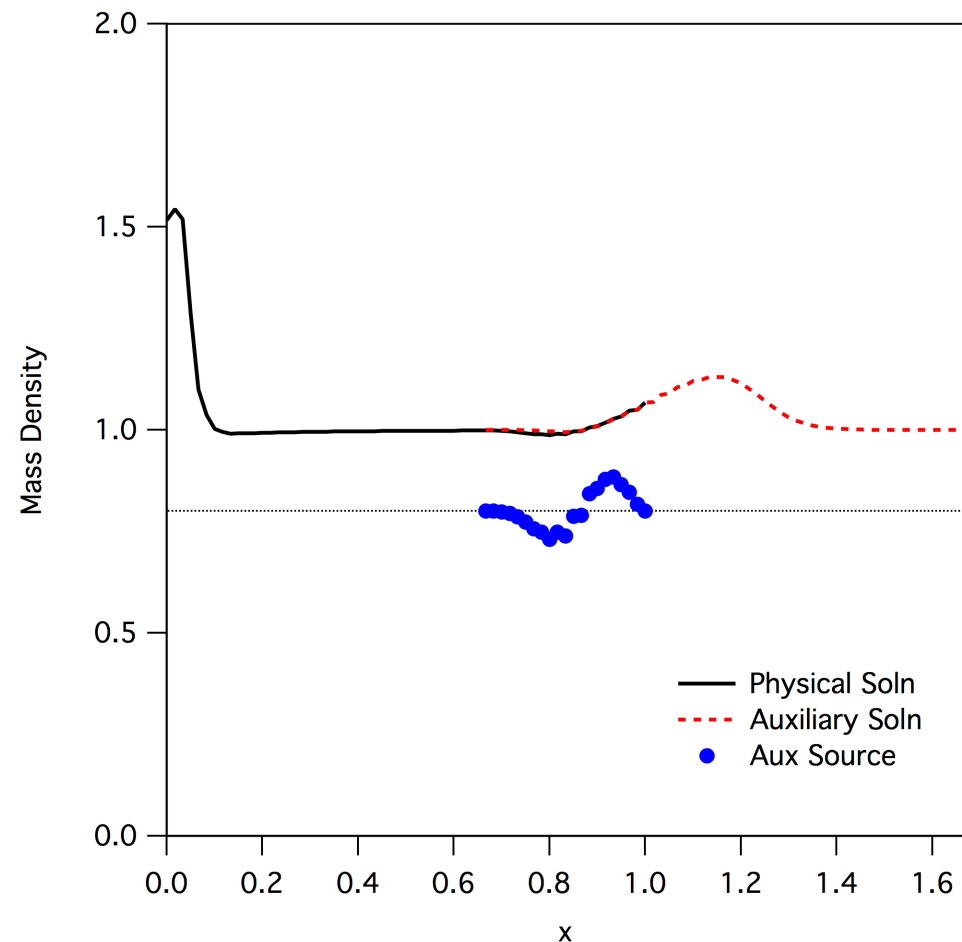
To demonstrate the effectiveness of the non-local boundary conditions, a 1D pulse is modeled using the Euler equations with thermal heat conduction.



Non-local boundary conditions demonstrated in 1D

Other methods have been used to reduce reflections, e.g. Riemann methods, PML. However, they are limited to normal incidence, purely hyperbolic, or problem-specific frequencies. The lacuna-based methods offer more versatility.

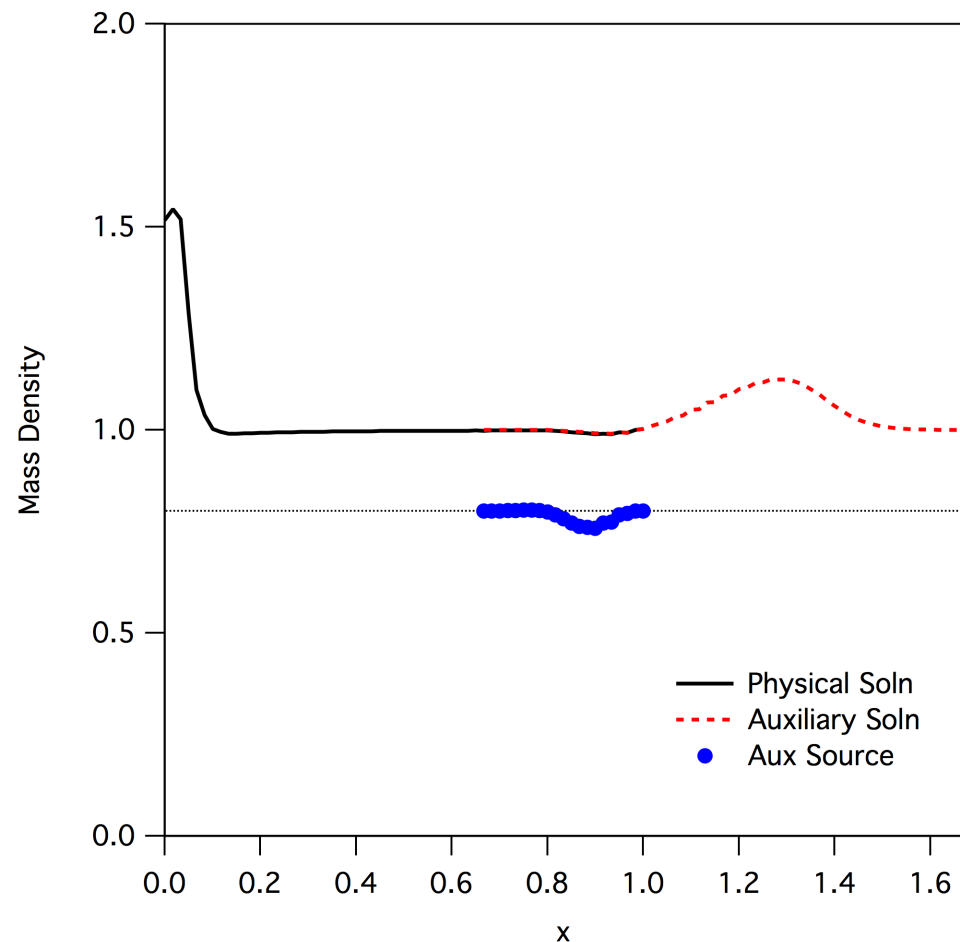
To demonstrate the effectiveness of the non-local boundary conditions, a 1D pulse is modeled using the Euler equations with thermal heat conduction.



Non-local boundary conditions demonstrated in 1D

Other methods have been used to reduce reflections, e.g. Riemann methods, PML. However, they are limited to normal incidence, purely hyperbolic, or problem-specific frequencies. The lacuna-based methods offer more versatility.

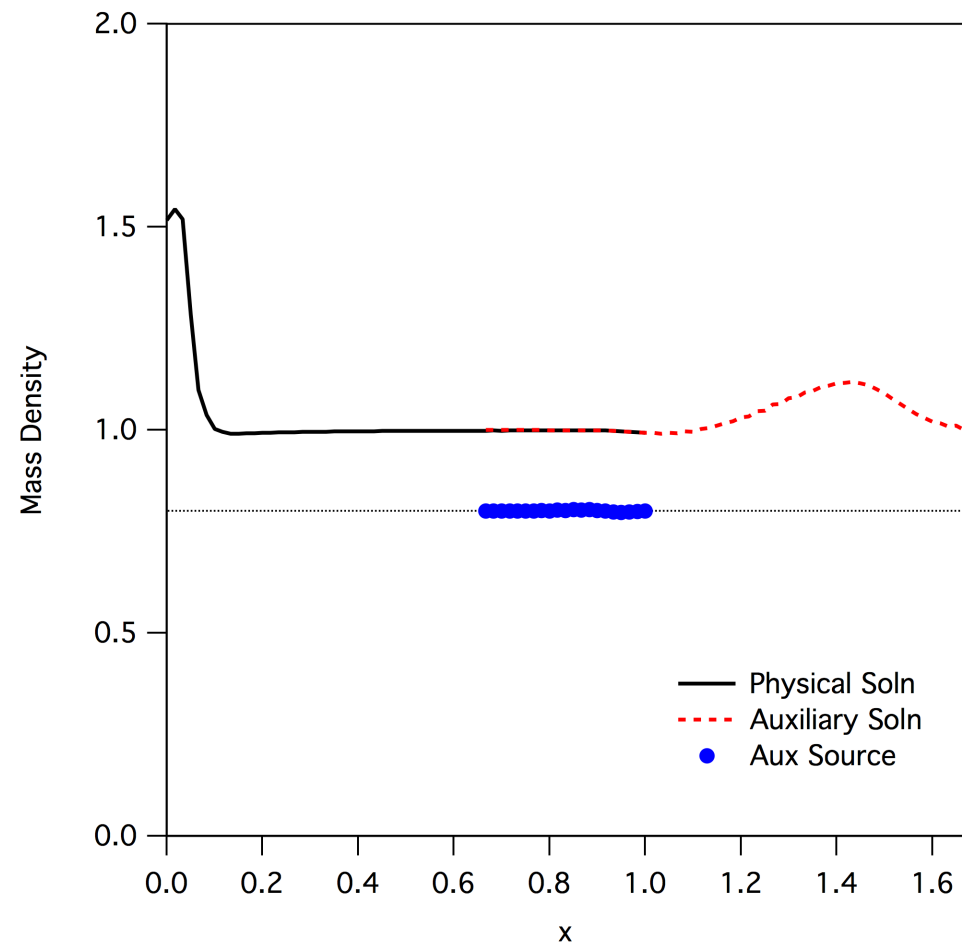
To demonstrate the effectiveness of the non-local boundary conditions, a 1D pulse is modeled using the Euler equations with thermal heat conduction.



Non-local boundary conditions demonstrated in 1D

Other methods have been used to reduce reflections, e.g. Riemann methods, PML. However, they are limited to normal incidence, purely hyperbolic, or problem-specific frequencies. The lacuna-based methods offer more versatility.

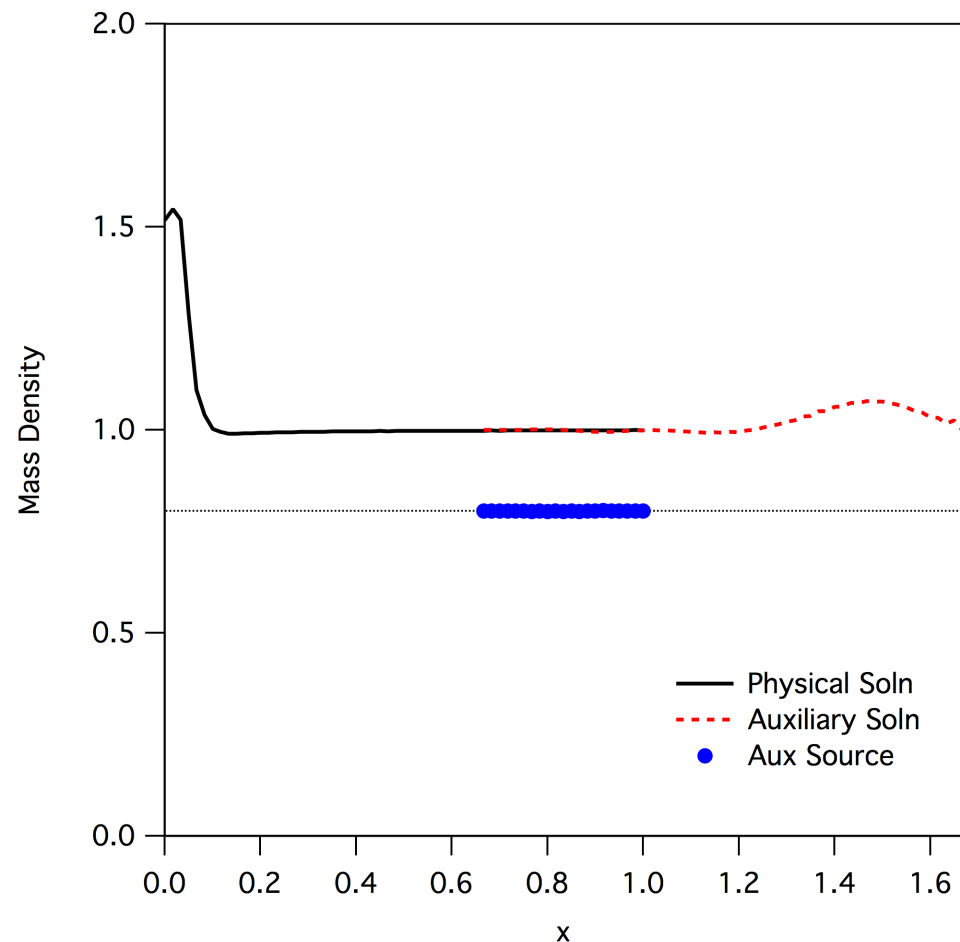
To demonstrate the effectiveness of the non-local boundary conditions, a 1D pulse is modeled using the Euler equations with thermal heat conduction.



Non-local boundary conditions demonstrated in 1D

Other methods have been used to reduce reflections, e.g. Riemann methods, PML. However, they are limited to normal incidence, purely hyperbolic, or problem-specific frequencies. The lacuna-based methods offer more versatility.

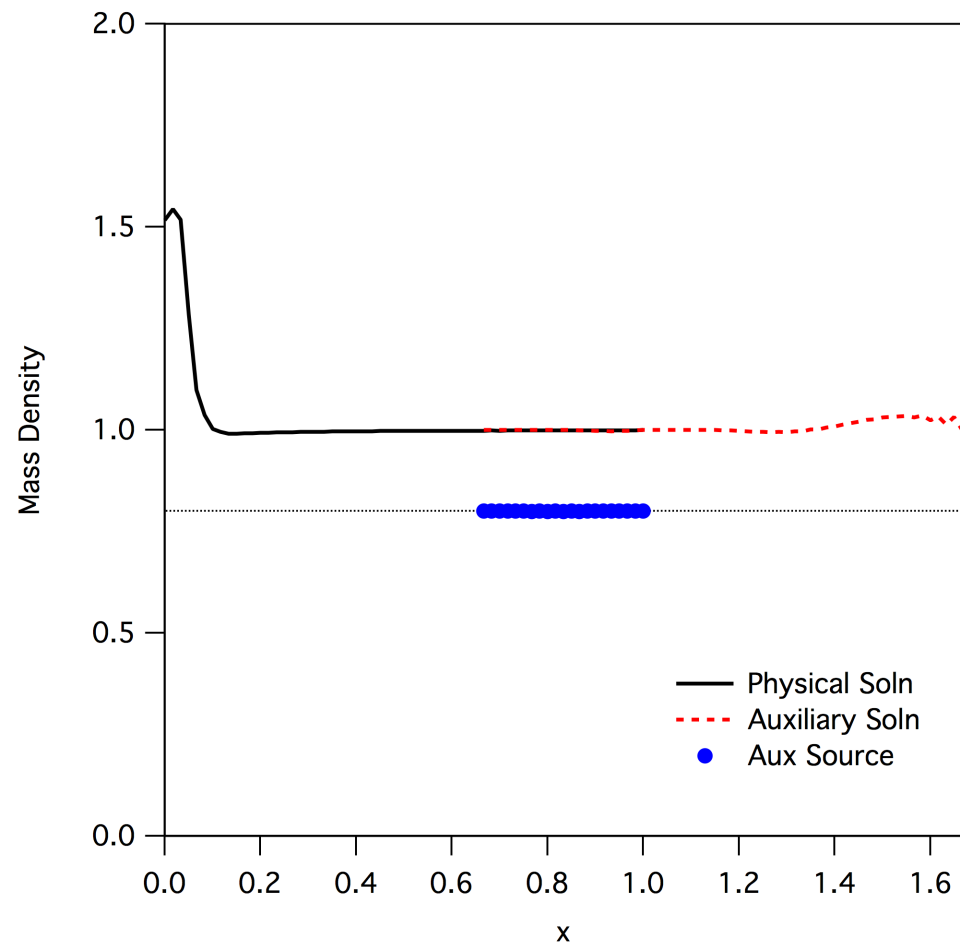
To demonstrate the effectiveness of the non-local boundary conditions, a 1D pulse is modeled using the Euler equations with thermal heat conduction.



Non-local boundary conditions demonstrated in 1D

Other methods have been used to reduce reflections, e.g. Riemann methods, PML. However, they are limited to normal incidence, purely hyperbolic, or problem-specific frequencies. The lacuna-based methods offer more versatility.

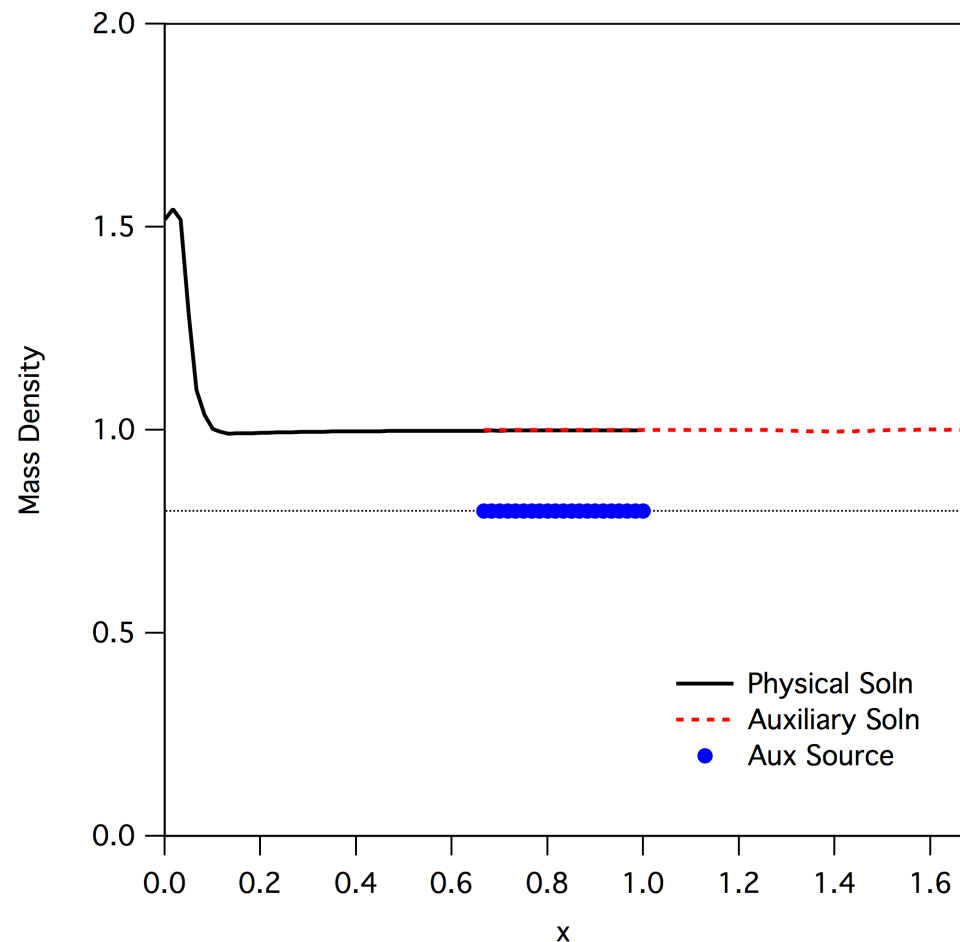
To demonstrate the effectiveness of the non-local boundary conditions, a 1D pulse is modeled using the Euler equations with thermal heat conduction.



Non-local boundary conditions demonstrated in 1D

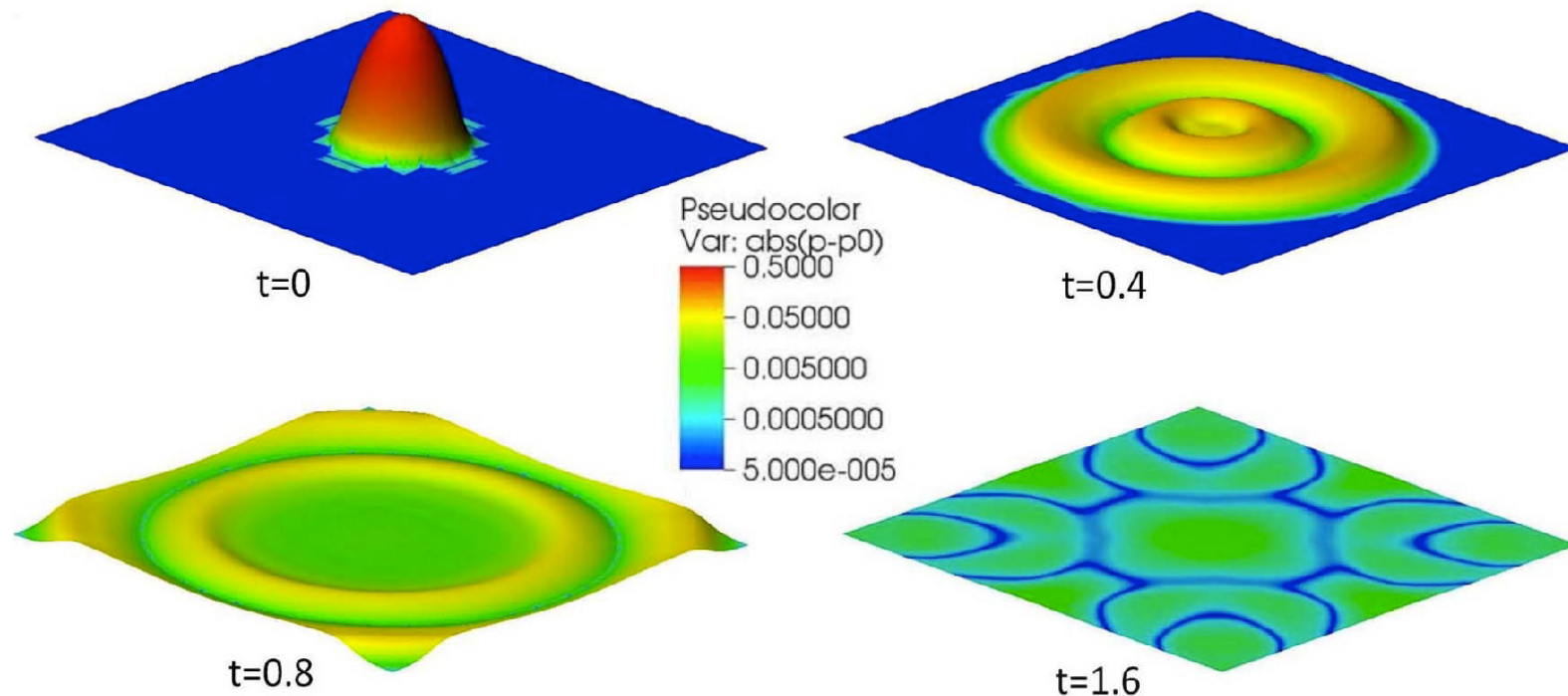
Other methods have been used to reduce reflections, e.g. Riemann methods, PML. However, they are limited to normal incidence, purely hyperbolic, or problem-specific frequencies. The lacuna-based methods offer more versatility.

To demonstrate the effectiveness of the non-local boundary conditions, a 1D pulse is modeled using the Euler equations with thermal heat conduction.



Lacuna-based open boundaries work even in 2D

The lacuna-based methods work for oblique incidence waves in either purely hyperbolic or mixed hyperbolic/parabolic systems. The method even works in 2D where there is no true lacuna. (Huygens' principle states true lacunae only exist in odd dimensional space.)

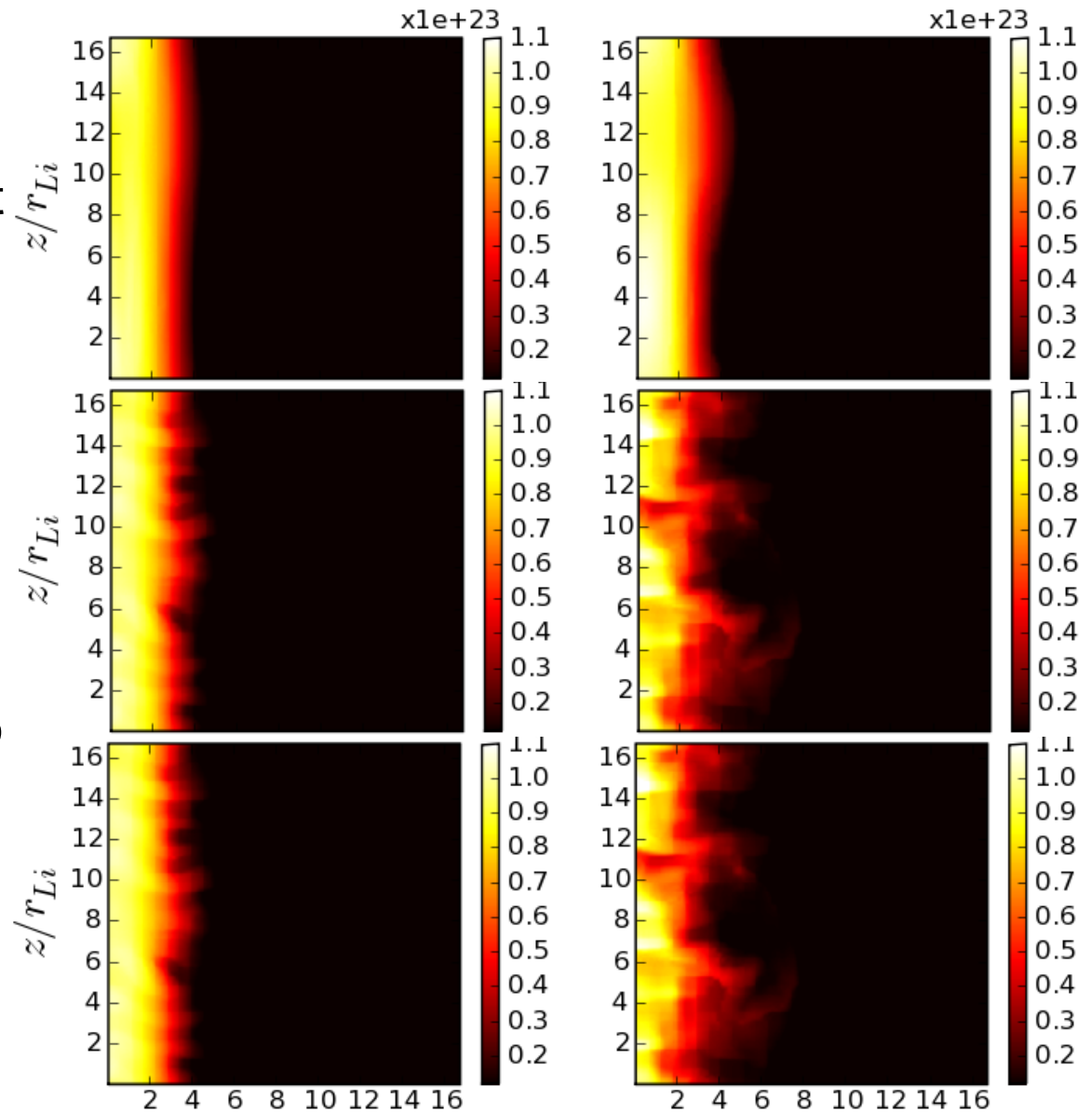


Shown is the nonlinear evolution of a 2D pressure pulse interacting with open boundaries on all sides.

Drift turbulence instabilities in a Z-pinch*

Z-pinch plasmas can exhibit drift turbulence instabilities when the drift speed exceeds the ion sound speed. This instability may explain the *anomalous resistivity* observed in many experiments.

Anomalous resistivity is also observed in FRC (Field Reversed Configuration) plasmas, such as the FRC experiment.

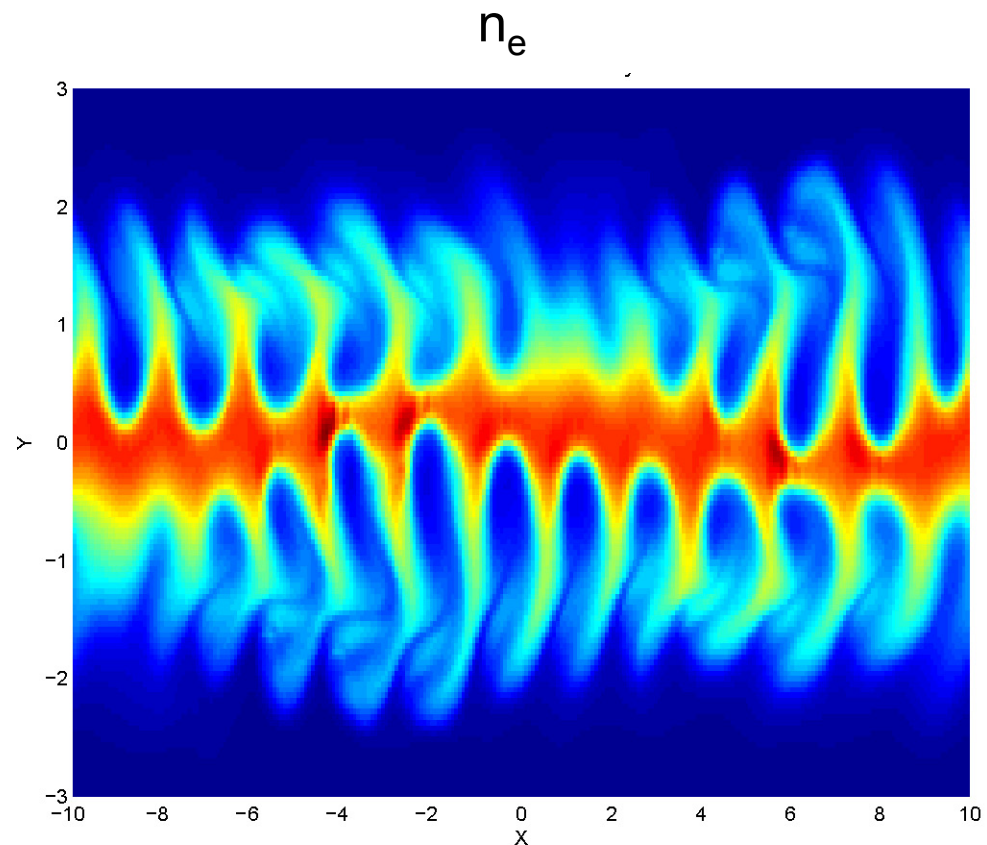


Anomalous resistivity in a Harris current sheet*

The same effect can be seen in a planar geometry in a Harris current sheet. The configuration has a horizontal current carried by a planar plasma. The Harris current sheet is ideal MHD stable.

The plasma develops the lower hybrid drift turbulence instability similar to the cylindrical Z-pinch configuration.

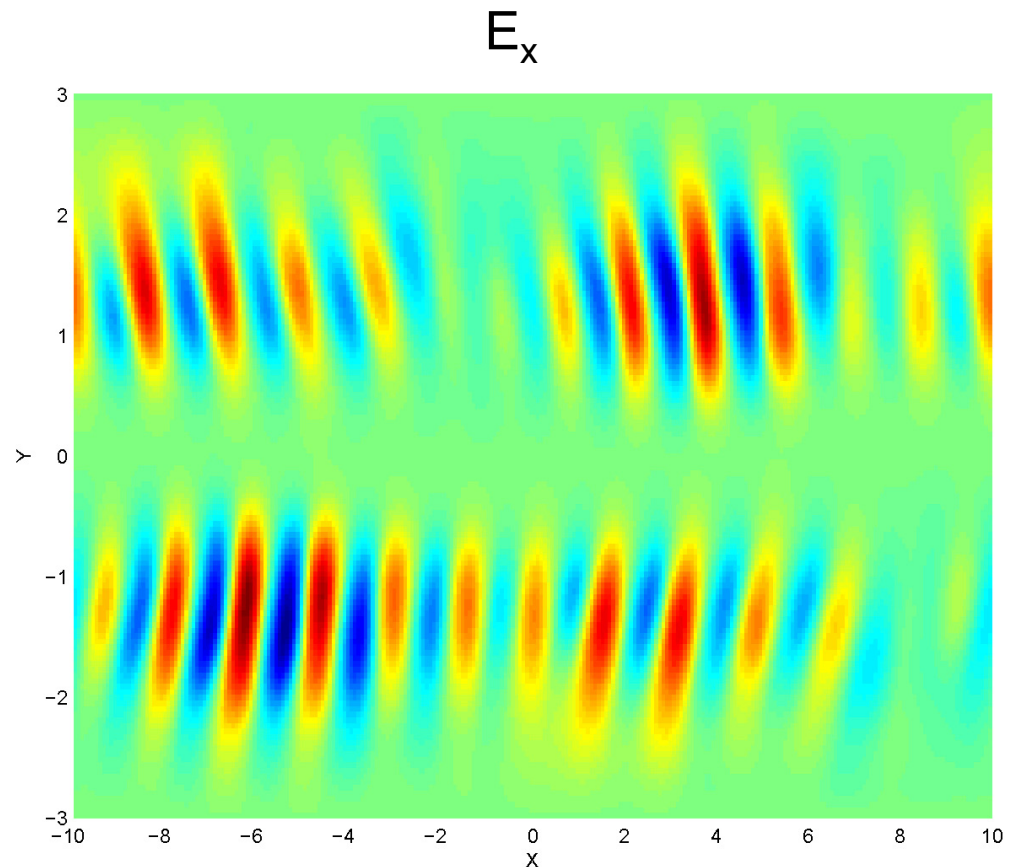
The mode develops along the density gradients and grows until saturation.



Anomalous resistivity in a Harris current sheet

The resulting charge separation effect of the instability can be seen from the large horizontal electric field that develops. In resistive MHD, this configuration would have an electric field that only varies in y .

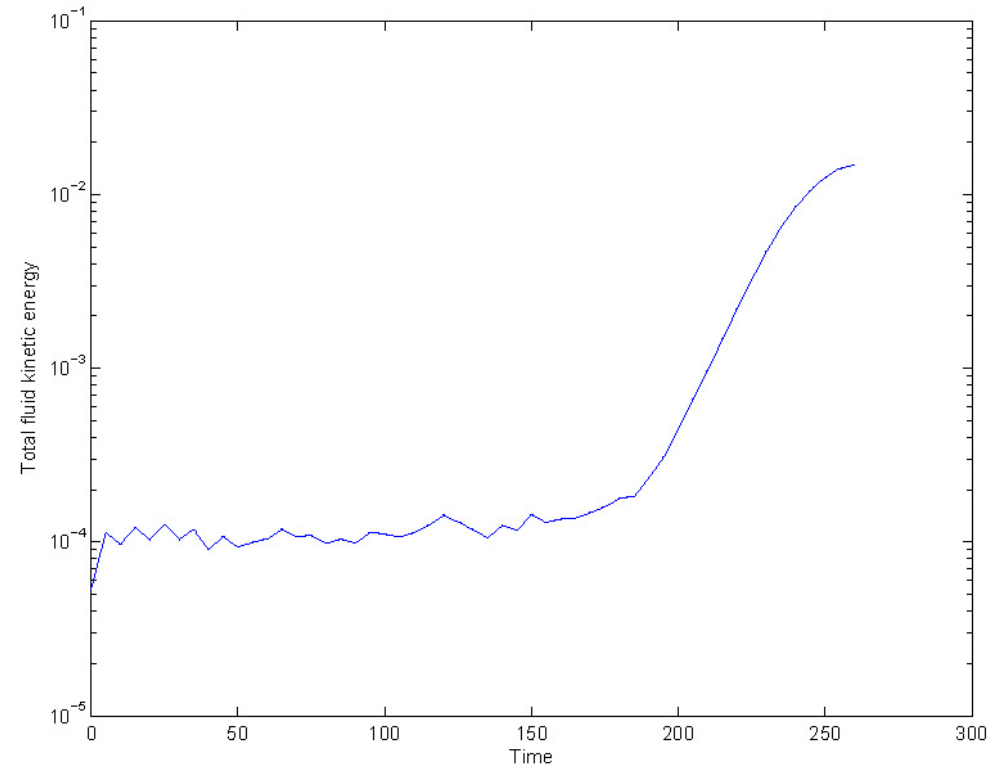
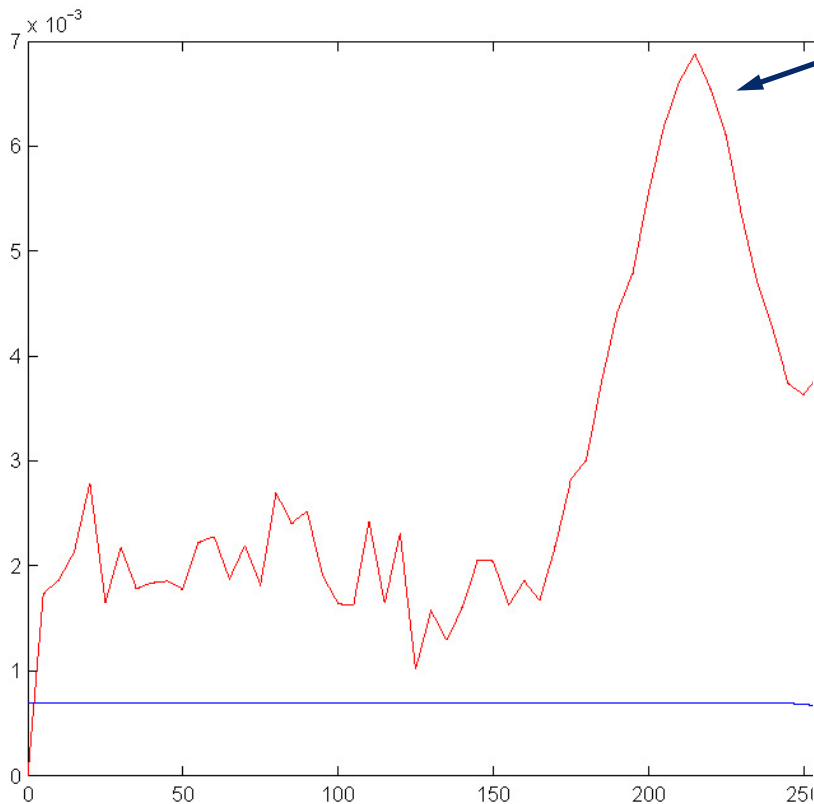
The electric field appears as an enhanced resistivity that is higher than the expected classical Spitzer resistivity.



Anomalous resistivity in the UW TCS FRC experiment

An effective resistivity can be computed and compared to the classical Spitzer resistivity.

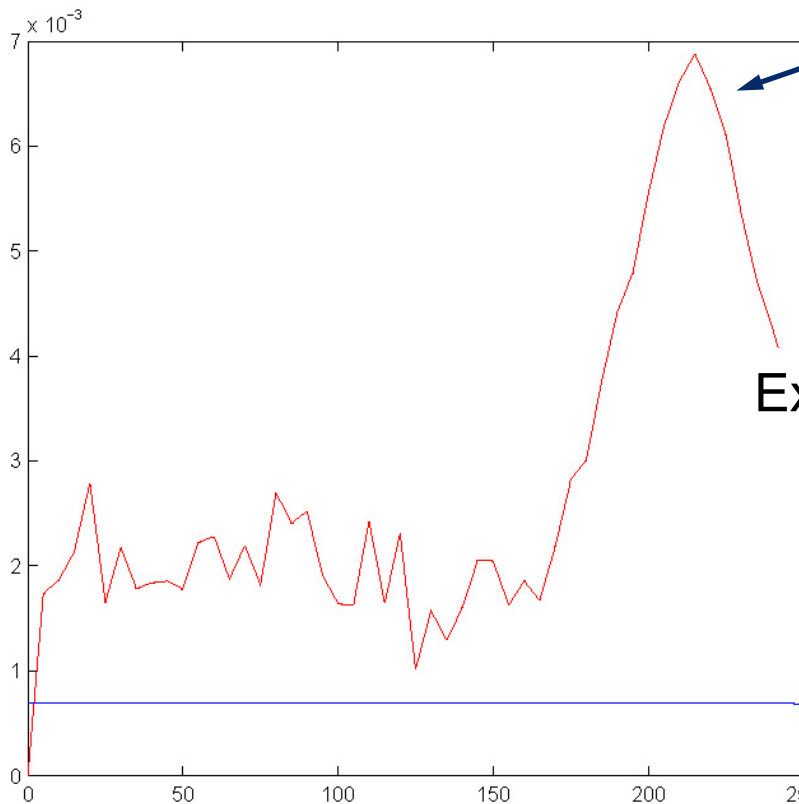
$$\eta_{\perp} = \int \mathbf{E} \cdot \mathbf{j} / \int \mathbf{j} \cdot \mathbf{j}$$



Anomalous resistivity in the UW TCS FRC experiment

An effective resistivity can be compared to the Spitzer resistivity.

$$\eta_{\perp} = \int \mathbf{E} \cdot \mathbf{j}$$



Experimental data from the UW TCS FRC measure an effective resistivity that compares well with the simulations.

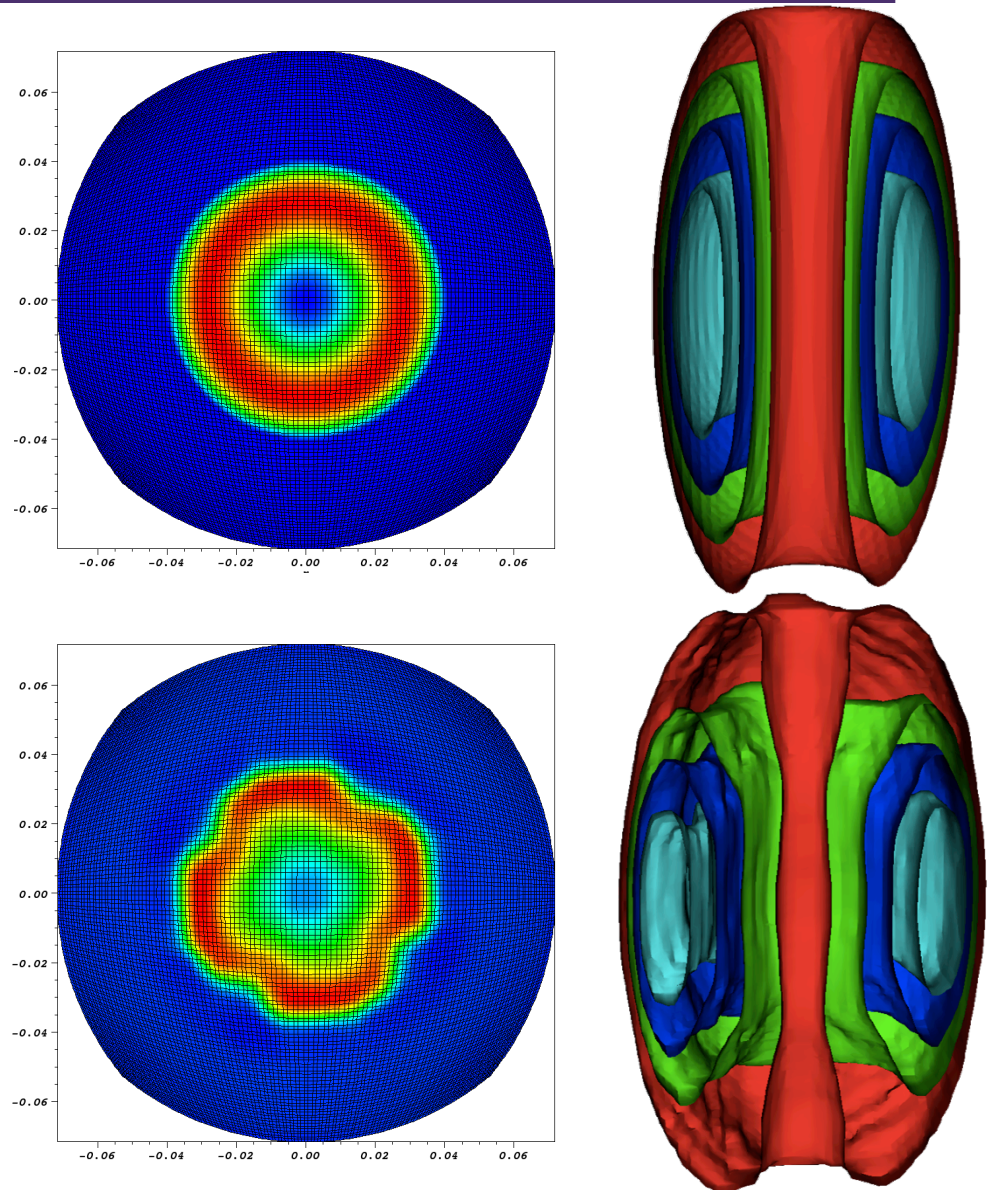
Pulse	V_{de} / V_{Thi}	$\eta_{\perp} / \eta_{\perp \text{ classical}}$
8966	2.22	11.12
8971	2.34	12.77
8997	2.32	7.97

3D, magnetically confined plasma simulations - FRC

FRCs form a toroidal equilibrium structure where plasma pressure is balanced by magnetic forces. Accurate balance of the hyperbolic fluxes and the source terms is essential.

FRC plasmas require two-fluid models for accuracy.

Electron drift produces an azimuthal current and poloidal magnetic fields. Cross-field drift can lead to a drift turbulence instability.

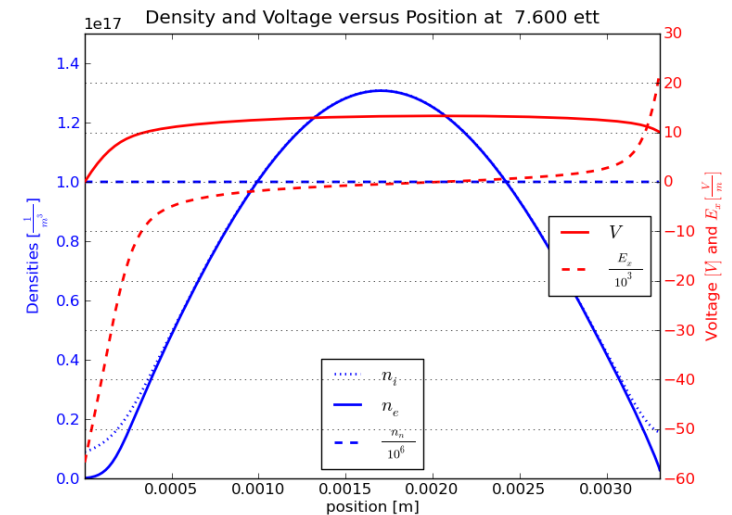
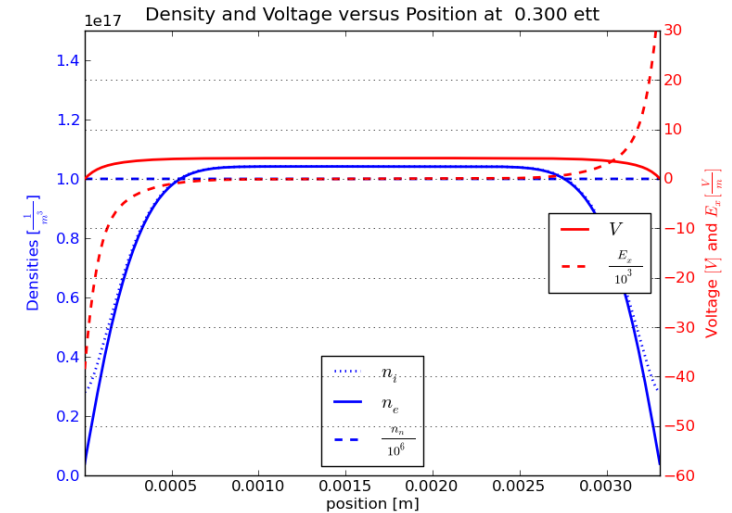
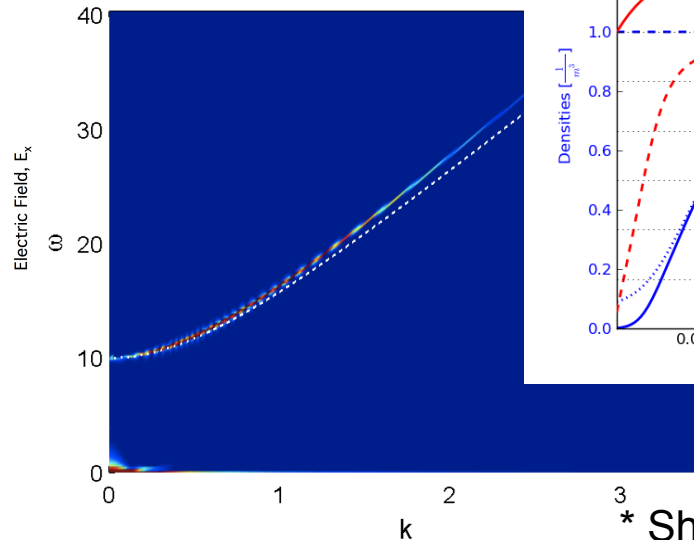
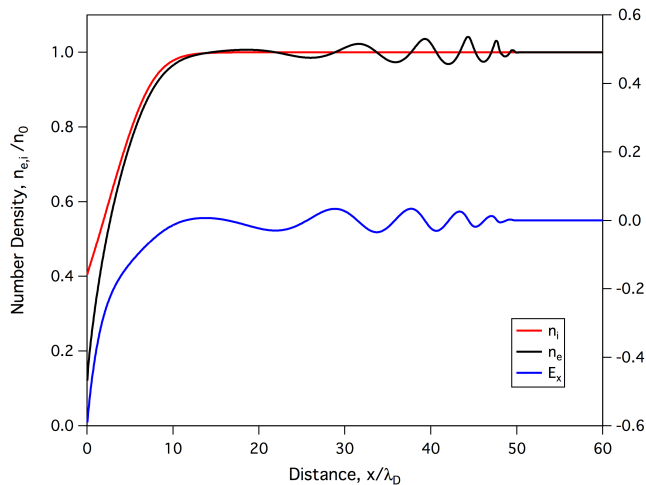


Self-consistent plasma sheath formation – reactions*

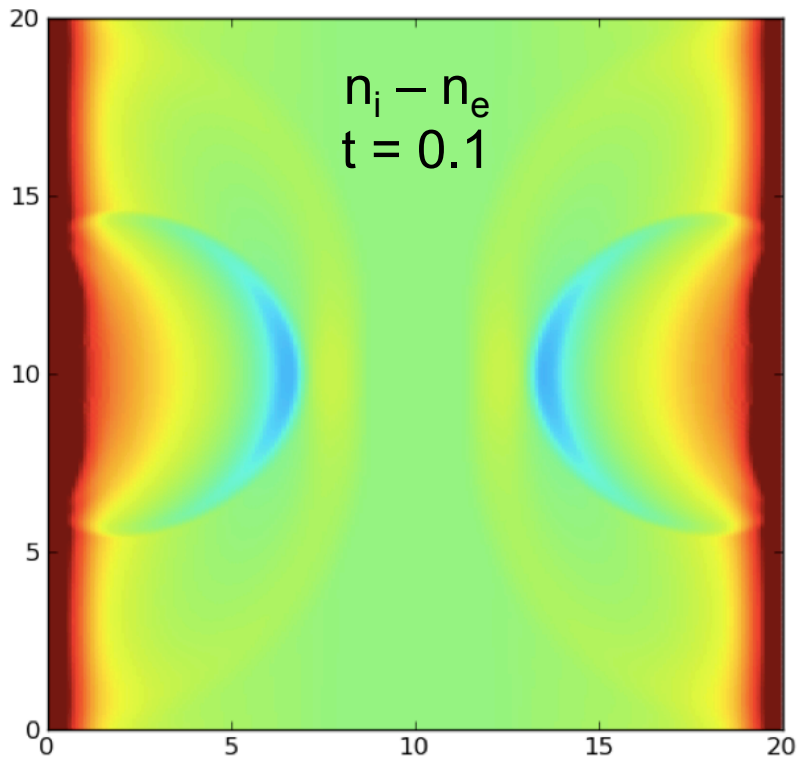
Three-fluid calculations provide self-consistent formation of plasma sheath which involves ionization and recombination physics. Since the model allows for electric fields and charge separation, external voltages can be applied.

Initial sheath formation shows Langmuir wave propagation.

$$\omega_L^2 = \omega_{pe}^2 + 1.5k^2 v_{Te}^2$$

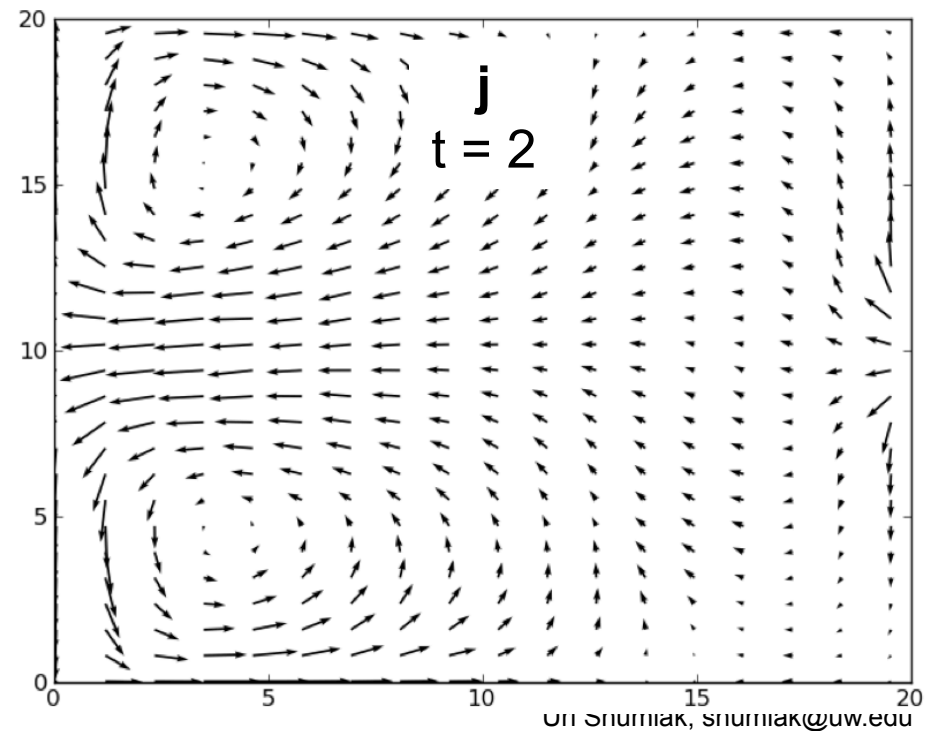


2D effects are evident, but Langmuir wave persists



2D effects can also be modeled for electrodes with finite extent, for realistic plasma configurations.

Langmuir waves propagate away from the electrodes during the initial plasma sheath formation.



When a quasi-steady-state is achieved, the current is carried mostly by electrons. Eddy currents are also visible.

Summary

- Moments of Boltzmann Eq. form foundation of multi-fluid plasma models.
- Scattering & reacting collisions and electromagnetic fields couple the multiple fluids to each other and to the fields.
- Usual asymptotic approximations simplify the governing model (Hall-MHD), but lead to unphysical wave behavior.
- High-order methods accurately compute equation system even when large source terms balance hyperbolic fluxes or strong anisotropies.
- Divergence relations of Maxwell's equations are satisfied either with purely hyperbolic treatment or with mixed potential formulation.
- Lacuna-based methods can robustly model open boundaries.
- Validation applications produce accurate, physically-expected results.
 - Drift turbulence instability related to anomalous resistivity
 - Ion, electron, neutral simulations of plasma sheath formation dynamics
- We have developed a high-order code for the multi-fluid plasma model called WARPX (Washington Approximate Riemann Plasma).